

¹ Study of the multi-strange resonance $\Xi(1530)^0$ production
² with ALICE at the LHC energies

³ Jihye Song

4 Contents

5	List of Figures	4
6	List of Tables	7
7	1 The physics of relativistic heavy-ion collisions	8
8	1.1 Standard model	8
9	1.2 Quantum Chromo-Dynamics	8
10	1.3 Heavy Ion Collisions	8
11	2 Production of resonance with strangeness	8
12	2.1 Resonance with strangeness	8
13	3 Theoretical models	8
14	3.1 Thermal statistical model	8
15	3.1.1 Calculations	10
16	3.1.2 Results	10
17	3.1.3 Comparison with data	12
18	3.2 UrQMD	12
19	4 A Large Ion Collider Experiment at the LHC	12
20	4.1 The Large Hadron Collider	13
21	4.2 The ALICE project	13
22	4.2.1 ALICE detector	13
23	4.2.2 Data Acquisition (DAQ) and trigger system	13
24	4.2.3 ALICE offline software frame work	13
25	5 Measurement of $\Xi(1530)^0$ production in p-Pb and Pb-Pb	13
26	5.1 $\Xi(1530)^0$ -reconstruction	14
27	5.1.1 Data sample and event selection	14
28	5.1.2 Track and topological selection	17
29	5.1.3 Particle identification	20
30	5.1.4 Signal extraction	23
31	5.2 Efficiency correction	32
32	5.3 Corrected p_T -spectra	35
33	5.4 Systematic uncertainties	37
34	5.5 $\Xi(1530)^0$ transverse momentum spectra	42
35	6 Results	42
36	6.1 Mean transverse momentum	42
37	6.2 Particle yield ratios	47

38	6.2.1	Comparison with other resonances	47
39	6.2.2	Comparison with models	47
40	References		47

⁴¹ **List of Figures**

42	1	Ratio of baryonic and mesonic resonances over their stable partner as a function of temperature.	11
44	2	Ratio of resonances over their stable partner as a function of $\sqrt(s)$	12
45	3	Vertex-z coordinate distribution of the accepted events in p–Pb collision(Left) and in Pb–Pb collisions(Right). The red dashed line indicates vertex cut .	15
47	4	Multiplicity distribution of accepted events in p–Pb collision in percentile. The each color and labels define the four intervals in which the analysis is performed.	16
50	5	Centrality distribution of three different trigger classes.	17
51	6	Sketch of the decay modes for Ξ^*0 and depiction of the track and topological selection criteria.	19
53	7	TPC dE/dx as function of transverse momentum for total (top) and selected first emitted π in 3σ (bottom)	20
55	8	TPC dE/dx as function of transverse momentum for total (top) and selected second emitted π in 3σ (bottom)	20
57	9	TPC dE/dx as function of transverse momentum for total (top) and selected last emitted π in 3σ (bottom)	21
59	10	TPC dE/dx as function of transverse momentum for total (top) and selected proton in 3σ (bottom)	21
61	11	TPC dE/dx as function of transverse momentum for total (top) and selected first emitted π in 3σ (bottom)	21
63	12	TPC dE/dx as function of transverse momentum for total (top) and selected second emitted π in 3σ (bottom)	22
65	13	TPC dE/dx as function of transverse momentum for total (top) and selected last emitted π in 3σ (bottom)	22
67	14	TPC dE/dx as function of transverse momentum for total (top) and selected proton in 3σ (bottom)	23
69	15	The $\Xi^\mp\pi^\pm$ invariant mass distribution (Same-event pairs) in $1.8 < p_T < 2.2 \text{ GeV}/c$ and for the multiplicity class 20-40%. The background shape, using pairs from different events (Mixed-event background), is normalised to the counts in $1.49 < M_{\Xi\pi} < 1.51 \text{ GeV}/c^2$ and $1.56 < M_{\Xi\pi} < 1.58 \text{ GeV}/c^2$	24
73	16	The $\Xi^\mp\pi^\pm$ invariant mass distribution (Same-event pairs) in $3.0 < p_T < 3.5 \text{ GeV}/c$ and for the centrality class 0-10%. The background shape, using pairs from different events (Mixed-event background), is normalised to the counts in $1.49 < M_{\Xi\pi} < 1.51 \text{ GeV}/c^2$ and $1.56 < M_{\Xi\pi} < 1.58 \text{ GeV}/c^2$	25
77	17	The invariant mass distribution after subtraction of the mixed-event background in p–Pb collisions. The solid curve represents the combined fit, while the dashed line describes the residual background.	26

80	18	The invariant mass distribution after subtraction of the mixed-event background in Pb–Pb collisions. The solid curve represents the combined fit, while the dashed line describes the residual background.	27
81	19	σ fit parameters as a function of p_{T} in MB in p–Pb collisions (top) and in Pb–Pb collisions (bottom).	29
82	20	$\Xi(1530)^0$ -mass obtained from fit of the Voigtian peak as a function of p_{T} in each multiplicity classes in p–Pb collisions (top) and the different centrality classes in Pb–Pb (bottom).	30
83	21	$\Xi(1530)^0$ -raw spectra obtained from fit of the Voigtian peak and a polynomial residual background for different multiplicities in p–Pb collisions (top) and Pb–Pb collisions (bottom). Only the statistical error is reported.	31
84	22	$\Xi(1530)^0$ -raw spectra obtained from fit of the Voigtian peak and a polynomial residual background for different multiplicities. Only the statistical error is reported.	32
85	23	Real corrected $\Xi(1530)^0$ spectrum (black) for the minimum bias with Levy fit (black curve). Also shown are the unweighted generated (blue) and reconstructed (red) $\Xi(1530)^0$ spectra.	33
86	24	Efficiency as a function of p_{T} in minimum bias events in p–Pb collisions.	34
87	25	Efficiency as a function of p_{T} in different centrality classes in Pb–Pb collisions	35
88	26	Corrected p_{T} -spectra of $\Xi(1530)^0$ in NSD and different multiplicity classes in p–Pb collisions.	36
89	27	Corrected p_{T} -spectra of $\Xi(1530)^0$ in different centrality classes in Pb–Pb collisions.	36
90	28	Summary of the contributions to the systematic uncertainty in minimum bias events in p–Pb collisions. The dashed black line is the sum in quadrature of all the contributions.	40
91	29	Systematic uncertainties for each multiplicity classes in p–Pb collisions.	40
92	30	Summary of the contributions to the systematic uncertainty in minimum bias events in Pb–Pb collisions. The dashed black line is the sum in quadrature of all the contributions.	41
93	31	Systematic uncertainties for each multiplicity classes.	41
94	32	Corrected yields as function of p_{T} in NSD events and multiplicity dependent event classes in p–Pb collision system. Statistical uncertainties are presented as bar and systematical uncertainties are plotted as boxes.	43
95	33	Corrected yields as function of p_{T} in different centrality classes in Pb–Pb collision system. Statistical uncertainties are presented as bar and systematical uncertainties are plotted as boxes.	44
96			
97			
98			
99			
100			
101			
102			
103			
104			
105			
106			
107			
108			
109			
110			
111			
112			
113			
114			
115			
116			

117	34	Mean transverse momenta $\langle p_T \rangle$ of Λ , Ξ^- , $\Sigma^{*\pm}$, Ξ^{*0} and Ω^- in p–Pb collisions at $\sqrt{s_{\text{NN}}} = 5.02$ TeV as a function of mean charged-particle multiplicity density $\langle dN_{\text{ch}}/d\eta_{\text{lab}} \rangle$, measured in the pseudorapidity range $ \eta_{\text{lab}} < 0.5$. The results for Λ , Ξ^- and Ω^- are taken from [1, 2, 3]. Statistical and systematic uncertainties are represented as bars and boxes, respectively. The Ω^- and Ξ^- points in the 3rd and 4th lowest multiplicity bins are slightly displaced along the abscissa to avoid superposition with the $\Xi(1530)^0$ points.	45
118			
119			
120			
121			
122			
123			
124	35	Mass dependence of the mean transverse momenta of identified particles for the 0 – 20% V0A multiplicity class and with $-0.5 < y_{\text{CMS}} < 0$ in p–Pb collisions at $\sqrt{s_{\text{NN}}} = 5.02$ TeV [1, 3], and in minimum-bias pp collisions at $\sqrt{s} = 7$ TeV [4] with $ y_{\text{CMS}} < 0.5$. Additionally, D^0 and J/ψ results are plotted. The D^0 and J/ψ were measured in different rapidity ranges: $ y_{\text{CMS}} < 0.5$ [5] ($ y_{\text{CMS}} < 0.9$ [6]) for D^0 (J/ψ) in pp and $-0.96 < y_{\text{CMS}} < 0.04$ [5] ($-1.37 < y_{\text{CMS}} < 0.43$ [7]) for D^0 (J/ψ) in p–Pb. Note also that the results for D^0 and J/ψ in p–Pb collisions are for the 0–100% multiplicity class.	46
125			
126			
127			
128			
129			
130			
131			
132	36	Integrated.	48
133	37	Integrated.	49
134			

¹³⁵ **List of Tables**

136	1	Parameters used in the thermal-model calculations.	9
137	2	Properties of particles used in the ratio calculations.	10
138	3	Difference of mass (ΔM), baryon number (ΔB), strangeness (ΔS) and charge (ΔQ) of the ratios. The values of the slopes needs to be checked!!!! .	12
139			
140	4	Number of accepted and analyzed events per multiplicity/centrality interval	17
141	5	Track selections common to all decay daughters and primary track selections applied to the charged pions from decays of Ξ^{*0}	18
142	6	Topological and track selection criteria.	18
143	7	Summary of the systematic uncertainties on the differential yield, $d^2N/(dp_T dy)$. Minimum and maximum values in all p_T intervals and multiplicity classes in p–Pb, centrality classes in Pb–Pb are shown for each source.	42
144			
145			
146			

147 **1 The physics of relativistic heavy-ion collisions**

148 This test for references [8]

149 **1.1 Standard model**

150 **1.2 Quantum Chromo-Dynamics**

151 **1.3 Heavy Ion Collisions**

152 **2 Production of resonance with strangeness**

153 **2.1 Resonance with strangeness**

154 **3 Theoretical models**

155 **3.1 Thermal statistical model**

156 The statistical-thermal model has proved extremely successful in applications to relativistic
157 collisions of both heavy ions and elementary particles. In light of this success, THERMUS,
158 a thermal model analysis package, has been developed for incorporation into the object-
159 oriented ROOT framework [9].

160
161 There are three types of statistical-thermal models in explaining data in high energy nu-
162 clear physics and THERMUS treats the system quantum numbers B (baryon number), S
163 (strangeness) and Q (charge) within three distinct formalisms:

164 1. **Grand-Canonical Ensemble:** Because the hot dense matter produced in nucleus-
165 nucleus collisions is large enough, this ensemble is the most widely used in applications
166 to heavy-ion collisions, in which the quantum numbers are conserved on average.

167 2. **Fully-Canonical Ensemble:** In which B, S and Q are each exactly conserved and
168 this ensemble used in high-energy elementary collisions such as pp, p \bar{p} and e $^-$ e $^+$
169 collisions.

170 3. **Strangeness-Canonical Ensemble:** In small systems or at low temperatures, a
171 canonical treatment leads to a suppression of hadrons carrying non-zero quantum
172 numbers, since these particles have to be created in pairs and the resulting low
173 production of strange particles requires a canonical treatment of strangeness.

174 In order to calculate the thermal properties of a system, one starts with an evaluation
175 of its partition function. The form of the partition function obviously depends on the
176 choice of ensemble. In the present analysis the strangeness-canonical ensemble used and
177 the statistical-thermal model requires six parameters as input: the chemical freeze-out

178 temperature T , baryon and charge chemical potentials μ_B and μ_Q respectively, canonical
179 or correlation radius, R_C ; the radius inside which strangeness is exactly conserved and the
180 fireball radius R . An additional strangeness saturation factor γ_S has been used as indicator
181 of a possible departure from equilibrium and $\gamma_S = 1.0$ corresponds to complete strangeness
182 equilibration.

183 The volume dependence cancels out when studying the particle ratios as well as strangeness
184 canonical equivalent to grand canonical formalism if $\Delta S = 0$ in the ratios and γ_S also can-
185 cels out. Parameters used in the analysis listed in Table 1. The μ_B parameter taken from
186 the Ref. [10].

Table 1: Parameters used in the thermal-model calculations.

Parameter	Value
T (MeV)	varied (see text)
μ_B (MeV)	$9.2 \times 10^{-2}????$
μ_Q (MeV)	0.0
γ_S	1.0

188 **3.1.1 Calculations**

189 *Concept:*

190 In order to calculate the particle ratios within strangeness canonical formalism of THER-
 191 MUS, temperature varied between 60 MeV to 180 MeV and particle yields extracted for
 192 each temperature value and then primary particle ratios calculated for each case.

193

194 *Feed-Down Correction:*

195 Since the particle yields measured by the detectors in collision experiments include feed-
 196 down from heavier hadrons and hadronic resonances, the primordial hadrons are allowed to
 197 decay to particles considered stable by the experiment before model predictions are com-
 198 compared with experimental data. In the analysis only Λ particles counted as stable (do not
 199 allowed to decay) so there is no feed-down contribution from these particles to the other
 200 ratios.

201

202

203 Properties of studied particles and their particle ratios listed in Table 2 and Table 3,
 204 respectively.

Table 2: Properties of particles used in the ratio calculations.

Particle	Δ^{++}	p	K^{*0}	K^0	K^+	Λ^*	Λ	Σ^{*+}	Σ^+	Σ^0
Mass (MeV/c^2)	1232	938.27	895.92	497.61	493.67	1519.5	1115.68	1382.8	1189.37	1192.6
Width (MeV/c^2)	120	–	50.7	–	–	15.6	–	37.6	–	–
$c\tau$ (fm)	1.6	–	3.9	–	–	12.6	–	5.51	–	–
Ang. Momentum (J)	3/2	1/2	1	1	0	3/2	1/2	3/2	1/2	1/2
Isospin (I)	3/2	1/2	1/2	1/2	1/2	0	0	1	1	1
Parity (P)	+1	+1	-1	-1	0	-1	+1	+1	+1	+1
Strangeness (S)	0	0	1	1	1	-1	-1	-1	-1	-1
Baryon Number (B)	1	1	0	0	0	1	1	1	1	1
Decay Channel	$p\pi^+$	–	π^-	–	$\mu^+\nu_\mu$	pK^-	$p\pi^-$	$\Lambda\pi^+$	$p\pi^0$	$\Lambda\gamma$
Branching Ratio (%)	~ 100	–	~ 66.7	–	~ 63.54	~ 45	~ 63.9	~ 87	~ 51.6	~ 100
Q-Value(MeV/c^2)	154.16	–	262.68	–	–	87.55	37.84	127.55	111.53	76.96

205

206

207 **3.1.2 Results**

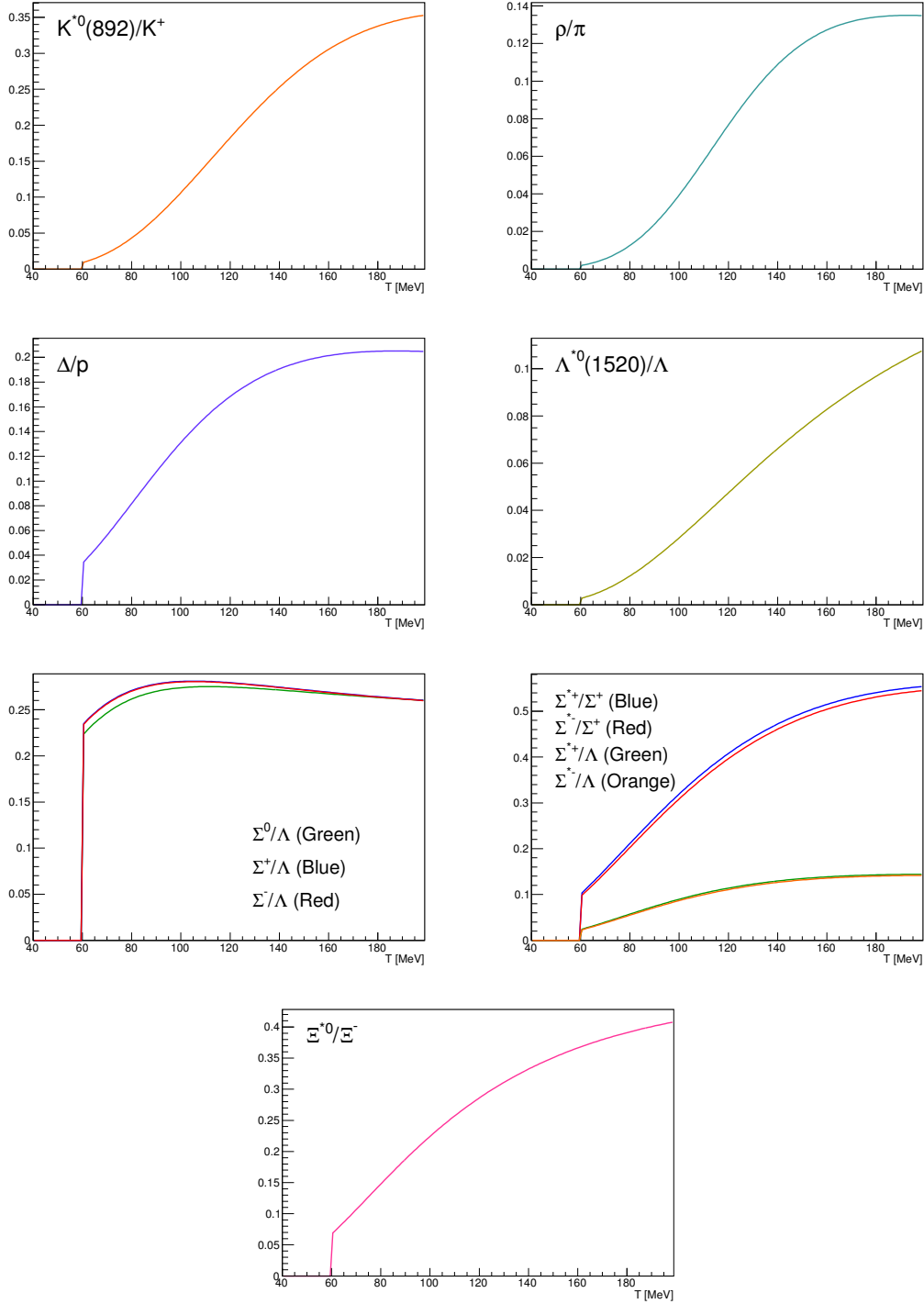


Figure 1: Ratio of baryonic and mesonic resonances over their stable partner as a function of temperature.

Table 3: Difference of mass (ΔM), baryon number (ΔB), strangeness (ΔS) and charge (ΔQ) of the ratios. The values of the slopes needs to be checked!!!!

Particle	Δ^{++}/p	K^*/K^+	Λ^*/Λ	Σ^{*+}/Λ	Σ^{*+}/Σ^0	Σ^0/Λ	Σ^{*+}/Σ^+	Ξ^{*0}/Ξ^-
ΔM (MeV/ c^2)	293.8	402.25	403.82	267.12	190.16	76.96	193.43	210.49
ΔB	0	0	0	0	0	0	0	0
ΔS	0	0	0	0	0	0	0	0
ΔQ	+1	-1	0	+1	0	+1	0	-1
Slope (%) per MeV ????????	0.19	0.76	0.98	0.25	-	-0.08	0.37	0.42

208 3.1.3 Comparison with data

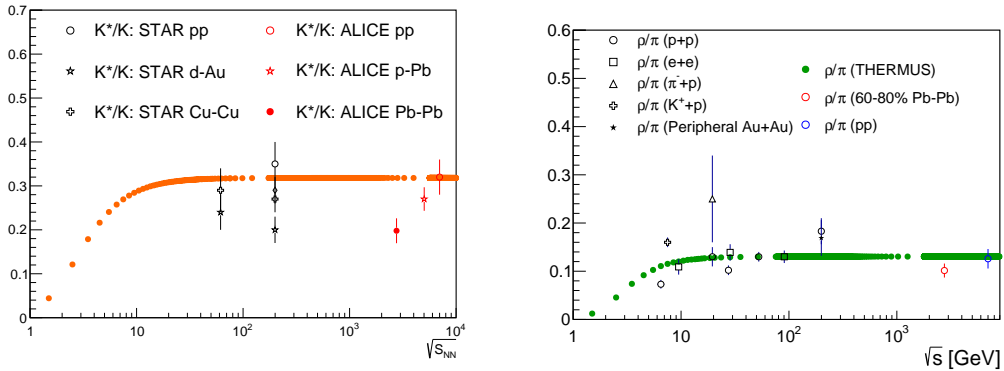


Figure 2: Ratio of resonances over their stable partner as a function of $\sqrt{(s)}$.

209 3.2 UrQMD

210 4 A Large Ion Collider Experiment at the LHC

211 ALICE (A Large Ion Collider Experiment) has been collecting data during the whole first
 212 phase of the Large Hadron Collider operations, from its startup on the 23 November 2009
 213 to the beginning of the first long technical shutdown in February 2013. During the first
 214 three years of operations LHC provided pp collisions at 0.9, 2.76, 7 and 8 TeV, Pb?Pb
 215 collisions at 2.76A TeV and finally p?Pb collisions at 5.02 TeV. The first section of this
 216 chapter focuses on the LHC performance during this phase and includes details on the
 217 accelerator parameters that allow the LHC to perform as a lead ion collider. A detailed
 218 description of the ALICE detector follows in the section 2.2. ALICE has been designed and

219 optimized to study the high particle-multiplicity environment of ultra-relativistic heavy-ion
220 collisions and its tracking and particle identification performance in Pb-Pb collisions are
221 discussed. The attention is drawn in particular on the central barrel detectors. Section
222 2.3 de- scribes the ALICE Data Acquisition (DAQ) system, that also embeds tools for the
223 online Data Quality Monitoring (DQM). The final part of the chapter is dedicated to the
224 offline computing and reconstruction system based on the GRID framework.

225 **4.1 The Large Hadron Collider**

226 The Large Hadron Collider (LHC) [57], [58] is a two-ring-superconducting hadron accel-
227 erator and collider installed in the 26.7 Km tunnel that hosted the LEP ma- chine and it
228 completes the CERN accelerator complex together with the PS and SPS, among the others
229 shown in fig. 2.1. Four main experiments are located in four different interaction points
230 along its circumference. ATLAS and CMS, the biggest ones, are multi-purpose detectors
231 built to discover the Higgs boson and hints of new physics beyond the Standard Model.
232 LHCb is dedicated to the physics of the flavour, focusing on the study CP-violation using B
233 meson decay channels. The phenomena that these three experiments aim to observe have
234 production cross sec- tion of the order of a hundred of pb or lower, therefore a large number
235 of collision events is required to the machine in order to fulfill the LHC pp physics program.
236 ALICE, on the contrary, is dedicated to the physics of Quark Gluon Plasma through the
237 observation of high-energy heavy-ion collisions, although a shorter physics pro- gram with
238 pp collisions has been carried out.

229 **4.2 The ALICE project**

240 **4.2.1 ALICE detector**

241 **4.2.2 Data Acquisition (DAQ) and trigger system**

242 **4.2.3 ALICE offline software frame work**

243 **5 Measurement of $\Xi(1530)^0$ production in p–Pb and Pb–Pb**

244 The measurement of resonance production in p–Pb collisions helps to disentangle cold
245 nuclear matter effects from genuine hot medium effects and contribute to the study of
246 the system size dependence of re-scattering in the hadronic phase. And the measurement
247 in ultra-relativistic heavy-ion collisions such as Pb–Pb collisions, provide information on
248 the properties of hadronic medium and different stage of its evolution. In order to study
249 the particle production mechanism in the hadronic phase between the chemical and ki-
250 netic freeze-out, the $\Xi(1530)^0$ resonance production at mid-rapidity($-0.5 < y_{\text{CMS}} < 0$) is
251 measured in p–Pb collisions $\sqrt{s_{\text{NN}}} = 5.02$ TeV and in Pb–Pb collisions with $|y| < 0.5$ at
252 $\sqrt{s_{\text{NN}}} = 2.76$ TeV with the ALICE experiment, via the reconstruction of its hadronic decay
253 into $\Xi\pi$.

254 **5.1 $\Xi(1530)^0$ -reconstruction**

255 The Ξ^{*0} production in p–Pb and Pb–Pb collisions at mid-rapidity has been studied in dif-
256 ferent multiplicity classes, from very central to peripheral collisions. The analysis strategy
257 is based on the invariant mass study of the reconstructed pairs (referred to as the candi-
258 dates) whose provenance could be the decay of a Ξ^{*0} baryon into charged particles. The
259 decay products (also called daughters in the text) are identified as oppositely charged Ξ and
260 π among the tracks reconstructed in the central barrel. The event selection, track selec-
261 tion and the particle identification strategy is described. The raw signal yield is extracted
262 by fitting the background-subtracted invariant mass distribution in several transverse mo-
263 mentum intervals. In order to extract the p_T -dependent cross section, these yields are
264 corrected for efficiency. The p_T -dependent correction due to the detector acceptance and
265 reconstruction efficiency, $(\text{Acc} \times \epsilon_{rec})(p_T)$, is computed from a Monte Carlo simulation.
266 The absolute normalisation is then performed, by dividing for the number of the events in
267 each multiplicity and centrality classes.

268 **5.1.1 Data sample and event selection**

269 A description of the ALICE detector and of its performance during the LHC Run 1 (2010–
270 2013) can be found in [11, 12]. The data sample in the analysis from Pb–Pb collisions with
271 energy of $\sqrt{s_{\text{NN}}}=2.76$ obtained during 2011 and the sample of p–Pb run at $\sqrt{s_{\text{NN}}}=5.02$
272 TeV was recorded in 2013.

273 Due to the asymmetric energies of the proton (4 TeV) and lead ion (1.57 A TeV) beams,
274 the centre-of-mass system in the nucleon-nucleon frame is shifted in rapidity by $\Delta y_{\text{NN}} =$
275 0.465 towards the direction of the proton beam with respect to the laboratory frame of
276 the ALICE detector [2]. For the analysed p–Pb data set, the direction of the proton beam
277 was towards the ALICE muon spectrometer, the so-called “C” side, standing for negative
278 rapidities; conversely, the Pb beam circulated towards positive rapidities, labelled as “A”
279 side in the following. The analysis in this paper was carried out at midrapidity, in the
280 rapidity window $-0.5 < y_{\text{CMS}} < 0$.

281 The minimum-bias trigger during the p–Pb run was configured to select events by
282 requiring a logical OR of signals in V0A and V0C [12], two arrays of 32 scintillator detectors
283 covering the full azimuthal angle in the pseudo-rapidity regions $2.8 < \eta_{\text{lab}} < 5.1$ and
284 $-3.7 < \eta_{\text{lab}} < -1.7$, respectively [13]. In the data analysis it was required to have a
285 coincidence of signals in both V0A and V0C in order to reduce the contamination from
286 single-diffractive and electromagnetic interactions. Out of this sample in p–Pb collision
287 events about 109.3 million events, 93.9 million events satisfy the following selection criteria
288 and have been actually used for the analysis.

289 The Pb–Pb collisions data sample was selected by online centrality trigger requiring a
290 signal in the forward V0 detectors[14] to record enhanced data in central collision. The
291 data consists of 24.8 million events in most central collisions (0-10%), 21.8 million events in
292 semi-central collisions (10-50%) and 3.5 million events with minimum-bas trigger (0-90%).

293 Among 49.6 million events in total, 43.0 million events have been analyzed as passed the
 294 criteria below.

- 295 • Events with z-coordinate of primary vertex (V_z) falling within ± 10 cm from the
 296 interaction point
- 297 • Rejection of pile-up event
- 298 • Requiring primary tracks to have at least one hit in one of the two innermost layers
 299 of the ITS (silicon pixel detector, SPD)
- 300 • p–Pb: multiplicity ranges in percentile (V0A): 0-20%, 20-40%, 40-60%, 60-100% and
 301 MB(0-100%)
- 302 • Pb–Pb: centrality classes (V0A and V0C): 0-10%, 10-40%, 40-80% and MB (0-80%)

303 The distribution of the vertex z position of the accepted events in p–Pb collision is
 304 reported on left panel in Figure 3 and corresponding figure but obtained from Pb–Pb
 305 collisions is shown on right panel in Figure. 3. Events with $|V_z| < 10$ cm have been used
 306 to ensure a uniform acceptance in the central pseudo-rapidity region, $|\eta| < 0.8$, where the
 307 analysis is performed. This cut reduces the total number of events to 97.5 million events,
 308 that is the $\sim 89.2\%$ of the initial sample in p–Pb collisions and 43.04 million events which
 309 is $\sim 86.8\%$ of the initial sample in Pb–Pb collisions are survived.

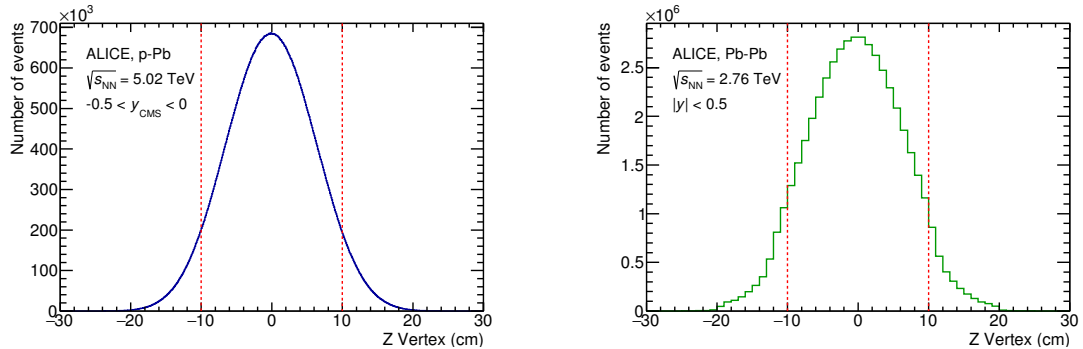


Figure 3: Vertex-z coordinate distribution of the accepted events in p–Pb collision(Left) and in Pb–Pb collisions(Right). The red dashed line indicates vertex cut

310 Fig. 4 shows the multiplicity distribution of the accepted events in p–Pb collision
 311 divided in bins of percentile. The each color on the histogram indicate the multiplicity
 312 ranges used in this analysis. Corresponding events for each multiplicity range are in Table
 313 4.

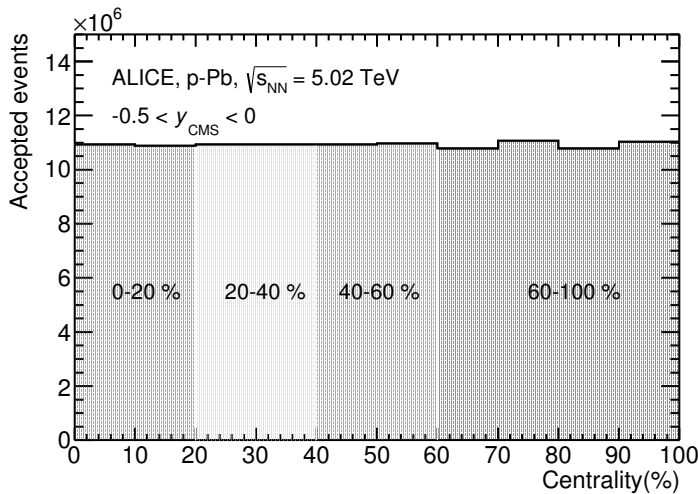


Figure 4: Multiplicity distribution of accepted events in p–Pb collision in percentile. The each color and labels define the four intervals in which the analysis in performed.

314 The distribution of centrality in each trigger used to select the events in Pb–Pb collision
 315 is shown in Fig. 5 and the reason why the centrality has step structure is that there are
 316 three different trigger classes classified by the amplitude threshold on VZERO detector.
 317 Because the distribution of events as function of centrality is not a flat, this may lead to
 318 additional bias, in particular when one needs to combine the results from different triggers.
 319 For example, events from 40-80% centrality bin have bias with high statistics in 40-60%. In
 320 order to avoid this effect, we have applied a flattening procedure to have flat distribution
 321 of events as function of centrality. A brief explanation of the method is below :

- 322 1. Histograms are obtained for the effective mass distribution in 1% centrality bins and
 323 for the centrality distribution

 324 2. The effective mass distributions are scaled in each 1% centrality bin by a factor:
 325 Factor = Nevent in 20-40% / 20 / Nevent in current 1% bin

 326 3. Each bin in the centrality distribution is scaled using the factor described above

 327 4. Histograms are added for centrality bins of interest: 0-10%, 10-40%, 40-80%, 0-80%

328 The resulting number of events in each centrality classes is summarized in Table 4.

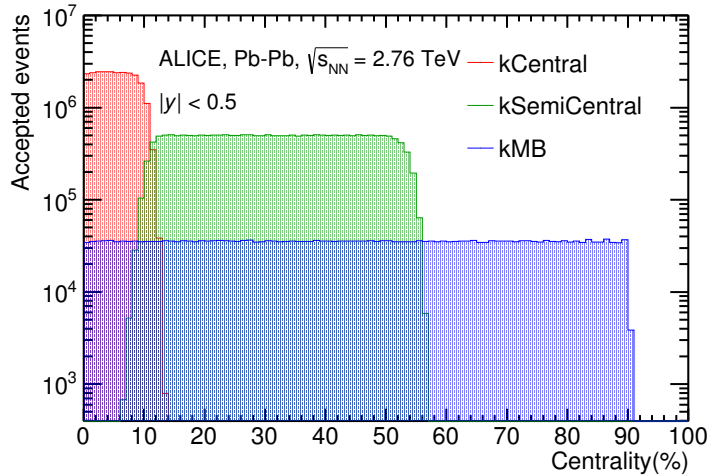


Figure 5: Centrality distribution of three different trigger classes.

p-Pb	0-20%	21.82×10^6
	20-40%	21.86×10^6
	40-60%	21.91×10^6
	60-100%	43.68×10^6
Pb-Pb	0-10%	5.58×10^6
	10-40%	16.73×10^6
	40-80%	22.31×10^6

Table 4: Number of accepted and analyzed events per multiplicity/centrality interval

329 5.1.2 Track and topological selection

330 In comparison with the Ξ^{*0} analysis carried out in pp collisions at $\sqrt{s} = 7$ TeV [4], track
 331 and topological selections were revised and adapted to the p-Pb dataset. Pions from strong
 332 decays of Ξ^{*0} were selected according to the criteria for primary tracks. As summarized
 333 in Table 5, all charged tracks were selected with $p_T > 0.15$ GeV/c and $|\eta_{\text{lab}}| < 0.8$,
 334 as described in Ref. [12]. The primary tracks were chosen with the Distance of Closest
 335 Approach (DCA) to PV of less than 2 cm along the longitudinal direction (DCA_z) and
 336 lower than $7\sigma_r$ in the transverse plane (DCA_r), where σ_r is the resolution of DCA_r . The σ_r
 337 is strongly p_T -dependent and lower than 100 μm for $p_T > 0.5$ GeV/c [12]. To ensure a good
 338 track reconstruction quality, candidate tracks were required to have at least one hit in one
 339 of the two innermost layers (SPD) of the ITS and to have at least 70 reconstructed points in

³⁴⁰ the Time Projection Chamber (TPC), out of a maximum of 159. The Particle IDentification
³⁴¹ (PID) criteria for all decay daughters are based on the requirement that the specific energy
³⁴² loss (dE/dx) is measured in the TPC within three standard deviations (σ_{TPC}) from the
expected value (dE/dx_{exp}), computed using a Bethe-Bloch parametrization [12].

Common track selections	$ \eta_{\text{lab}} $	< 0.8
	p_T	$> 0.15 \text{ GeV}/c$
	PID $ (\text{d}E/\text{d}x) - (\text{d}E/\text{d}x)_{\text{exp}} $	$< 3 \sigma_{\text{TPC}}$
Primary track selections	DCA_z to PV	$< 2 \text{ cm}$
	DCA_r to PV	$< 7\sigma_r - 10\sigma_r (p_T)$
	number of SPD points	≥ 1
	number of TPC points	> 70
	χ^2 per cluster	< 4

Table 5: Track selections common to all decay daughters and primary track selections applied to the charged pions from decays of Ξ^{*0} .

³⁴³ Since pions and protons from weak decay of Λ ($c\tau = 7.89 \text{ cm}$ [15]) and pions from weak
³⁴⁴ decay of Ξ^- ($c\tau = 4.91 \text{ cm}$ [15]) are produced away from the PV, specific topological and
³⁴⁵ track selection criteria, as summarized in Table 6, were applied [3, 4, 16].

Topological cuts	p–Pb	Pb–Pb
DCA_r of Λ decay products to PV	$> 0.06 \text{ cm}$	$> 0.11 \text{ cm}$
DCA between Λ decay products	$< 1.4 \text{ cm}$	$< 0.95 \text{ cm}$
DCA of Λ to PV	$> 0.015 \text{ cm}$	> 0.06
$\cos\theta_\Lambda$	> 0.875	> 0.998
$r(\Lambda)$	$0.2 < r(\Lambda) < 100 \text{ cm}$	$0.2 < r(\Lambda) < 100 \text{ cm}$
$ M_{p\pi} - m_\Lambda $	$< 7 \text{ MeV}/c^2$	$< 7 \text{ MeV}/c^2$
DCA_r of pion (from Ξ^-) to PV	$> 0.015 \text{ cm}$	$> 0.035 \text{ cm}$
DCA between Ξ^- decay products	$< 1.9 \text{ cm}$	< 0.275
$\cos\theta_\Xi$	> 0.981	> 0.9992
$r(\Xi^-)$	$0.2 < r(\Xi^-) < 100 \text{ cm}$	$0.2 < r(\Xi^-) < 100 \text{ cm}$
$ M_{\Lambda\pi} - m_\Xi $	$< 7 \text{ MeV}/c^2$	$< 7 \text{ MeV}/c^2$

Table 6: Topological and track selection criteria.

³⁴⁷ In the analysis of Ξ^{*0} , Λ and π from Ξ^- were selected with a DCA of less than 1.9 cm
³⁴⁸ and with a DCA_r to the PV greater than 0.015 cm. The Λ daughter particles (π and p)
³⁴⁹ were required to have a DCA_r to the PV greater than 0.06 cm, while the DCA between the
³⁵⁰ two particles was required to be less than 1.4 cm. Cuts on the invariant mass, the cosine

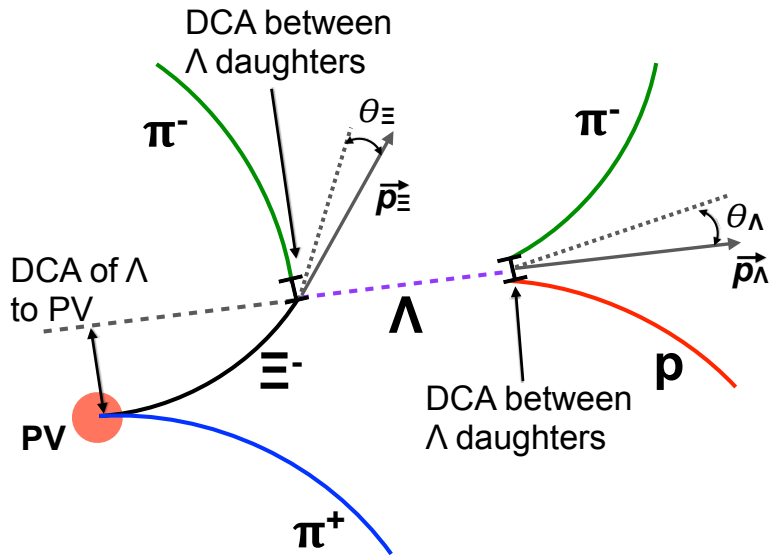


Figure 6: Sketch of the decay modes for Ξ^{*0} and depiction of the track and topological selection criteria.

³⁵¹ of the pointing angle ($\theta_\Lambda, \theta_\Xi$) and the radius of the fiducial volume ($r(\Lambda), r(\Xi)$) in Table 6
³⁵² were applied to optimize the balance of purity and efficiency of each particle sample.

353 **5.1.3 Particle identification**

354 PID selection criteria are applied for

- 355 1. π^\pm (last emitted π) and proton from Λ
356 2. π^\pm (second emitted π) from Ξ^\pm
357 3. π^\pm (first emitted π) from $\Xi(1530)^0$

358 by using TPC. On TPC dE/dx versus momentum distribution, 3σ cuts are applied to TPC
359 for selecting each of the particles. The TPC dE/dx selection allows to have better signal
360 with $\sim 20\%$ increase of significance.

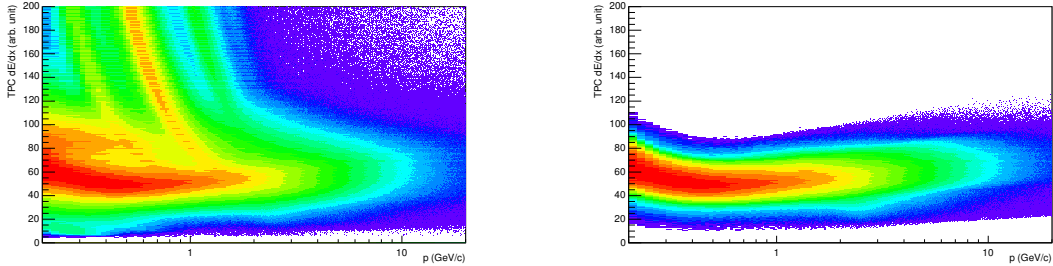


Figure 7: TPC dE/dx as function of transverse momentum for total (top) and selected first emitted π in 3σ (bottom)

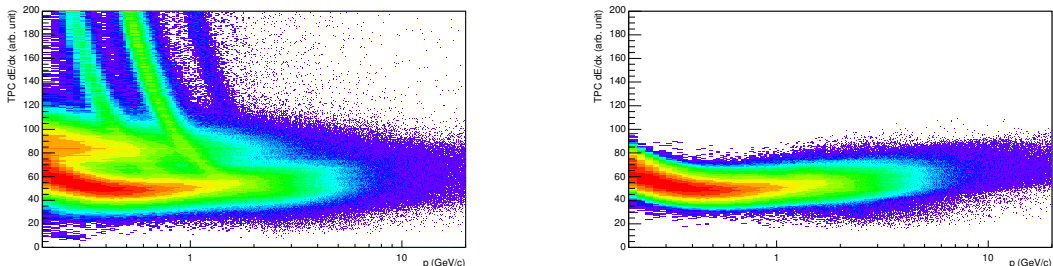


Figure 8: TPC dE/dx as function of transverse momentum for total (top) and selected second emitted π in 3σ (bottom)

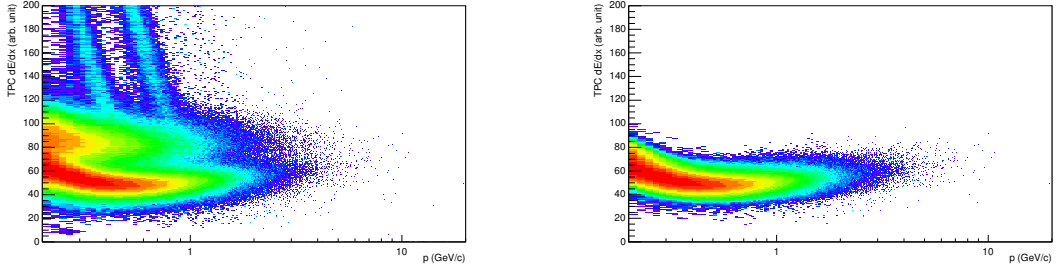


Figure 9: TPC dE/dx as function of transverse momentum for total (top) and selected last emitted π in 3σ (bottom)

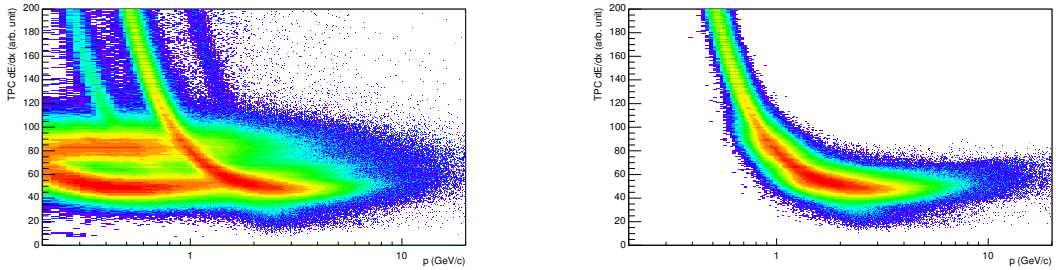


Figure 10: TPC dE/dx as function of transverse momentum for total (top) and selected proton in 3σ (bottom)

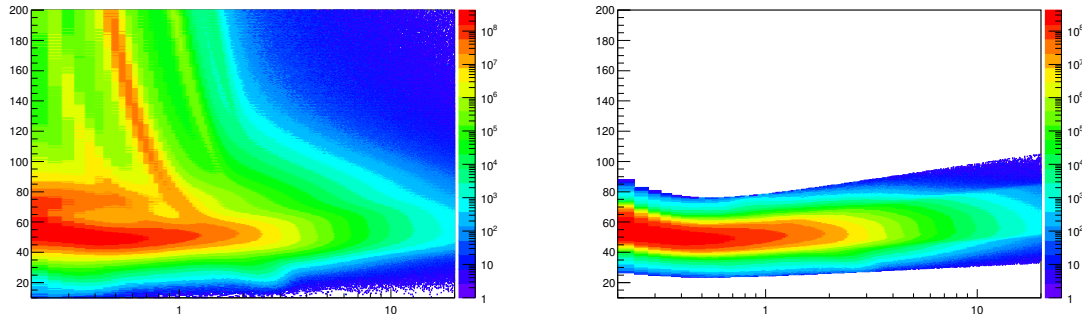


Figure 11: TPC dE/dx as function of transverse momentum for total (top) and selected first emitted π in 3σ (bottom)

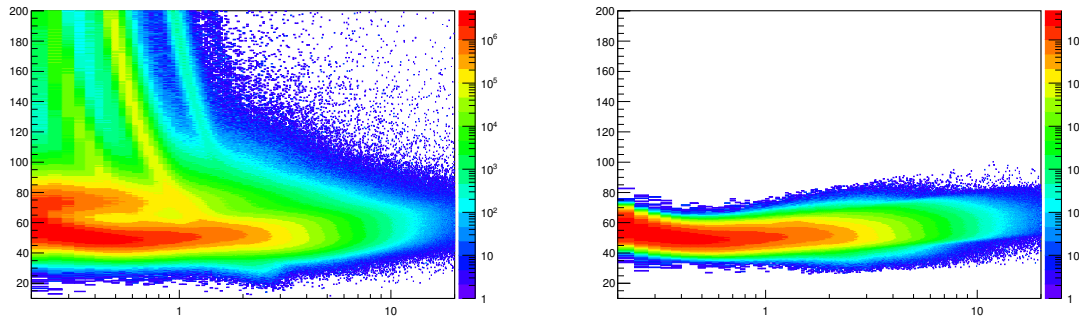


Figure 12: TPC dE/dx as function of transverse momentum for total (top) and selected second emitted π in 3σ (bottom)

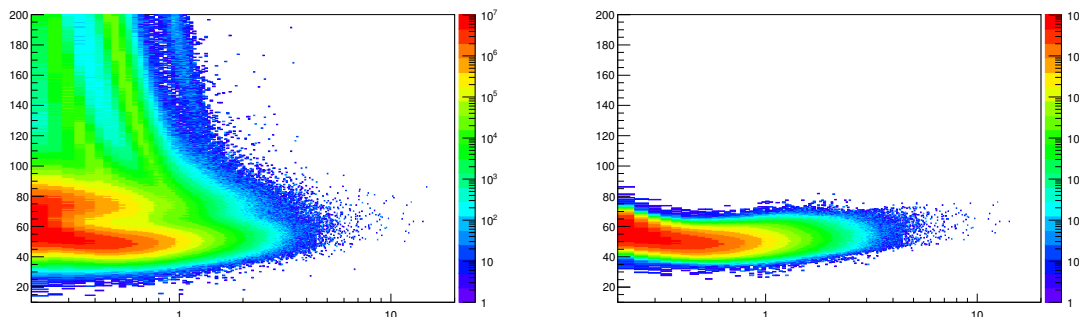


Figure 13: TPC dE/dx as function of transverse momentum for total (top) and selected last emitted π in 3σ (bottom)

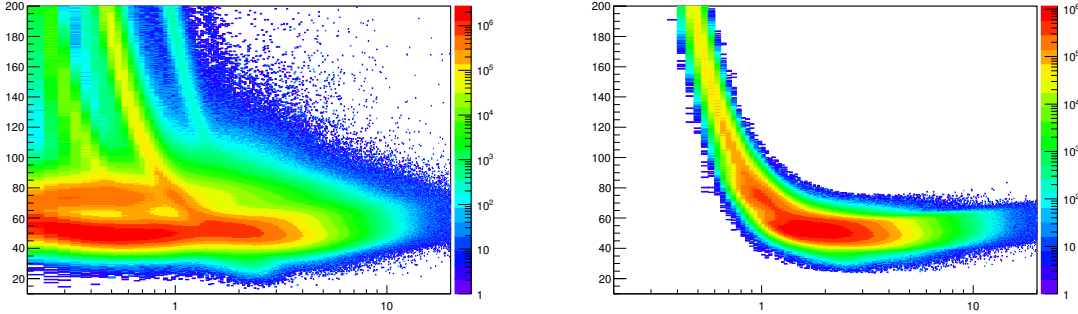


Figure 14: TPC dE/dx as function of transverse momentum for total (top) and selected proton in 3σ (bottom)

361 5.1.4 Signal extraction

362 The Ξ^{*0} signals were reconstructed by invariant-mass analysis of candidates for the decay
 363 products in each transverse momentum interval of the resonance particle, and for each
 364 multiplicity class. The $\Xi^-\pi^+(\Xi^+\pi^-)$ invariant mass distribution is reported in Figure 5.1.4
 365 for semi-central events (20-40%) in p-Pb collisions and Figure 5.1.4 for central events(0-
 366 10%) in Pb-Pb collisions.

367 Since the resonance decay products originate from a position which is indistinguishable
 368 from the PV, a significant combinatorial background is present. In order to extract
 369 $\Xi(1530)^0$ signal it is necessary to remove or, at least reduce, the combinatorial background.
 370 For this analysis, this has been done with the event mixing (EM) technique, by combining
 371 uncorrelated decay products 20 different events in p-Pb (5 different events in Pb-Pb). The
 372 events for the mixing have been selected by applying the similarity criteria to minimise
 373 distortions due to different acceptances and to ensure a similar event structure, only tracks
 374 from events with similar vertex positions z ($|\Delta z| < 1$ cm) and track multiplicities n ($|\Delta n| <$
 375 10) were taken.

376 The mixed-event background distributions were normalised to two fixed regions,
 377 $1.49 < M_{\Xi\pi} < 1.51 \text{ GeV}/c^2$ and $1.56 < M_{\Xi\pi} < 1.58 \text{ GeV}/c^2$, around the Ξ^{*0} mass
 378 peak (Figure 5.1.4 and 5.1.4). These regions were used for all p_T intervals and multiplicity
 379 classes, because the background shape is reasonably well reproduced in these regions and
 380 the invariant-mass resolution of the reconstructed peaks appears stable, independently of
 381 p_T . The uncertainty on the normalisation was estimated by varying the normalisation
 382 regions and is included in the quoted systematic uncertainty for the signal extraction (Section 5.4).

384 After the background subtraction, the resulting distribution is shown in Figure 5.1.4
 385 and 5.1.4. In order to obtain raw yields, a combined fit of a first-order polynomial for

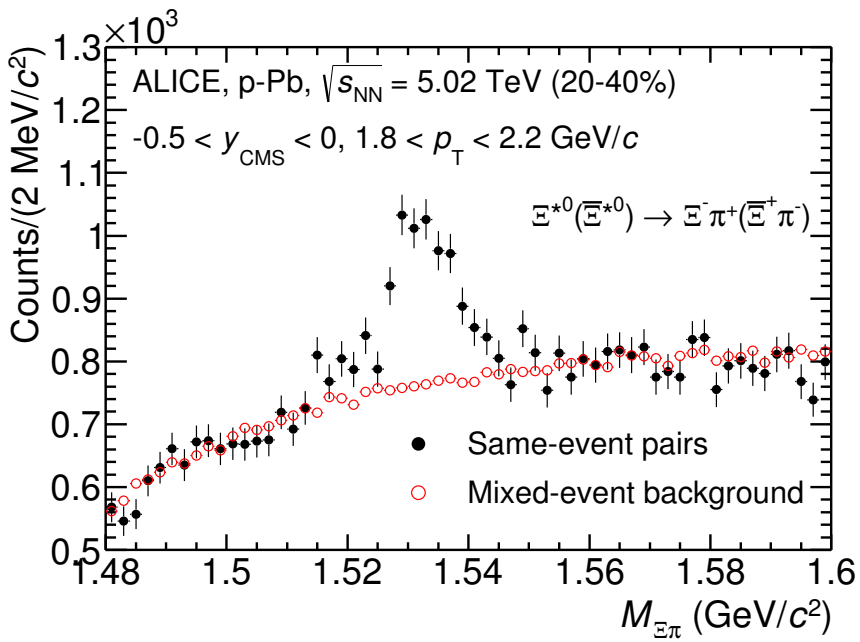


Figure 15: The $\Xi^\mp\pi^\pm$ invariant mass distribution (Same-event pairs) in $1.8 < p_{\text{T}} < 2.2 \text{ GeV}/c$ and for the multiplicity class 20-40%. The background shape, using pairs from different events (Mixed-event background), is normalised to the counts in $1.49 < M_{\Xi\pi} < 1.51 \text{ GeV}/c^2$ and $1.56 < M_{\Xi\pi} < 1.58 \text{ GeV}/c^2$.

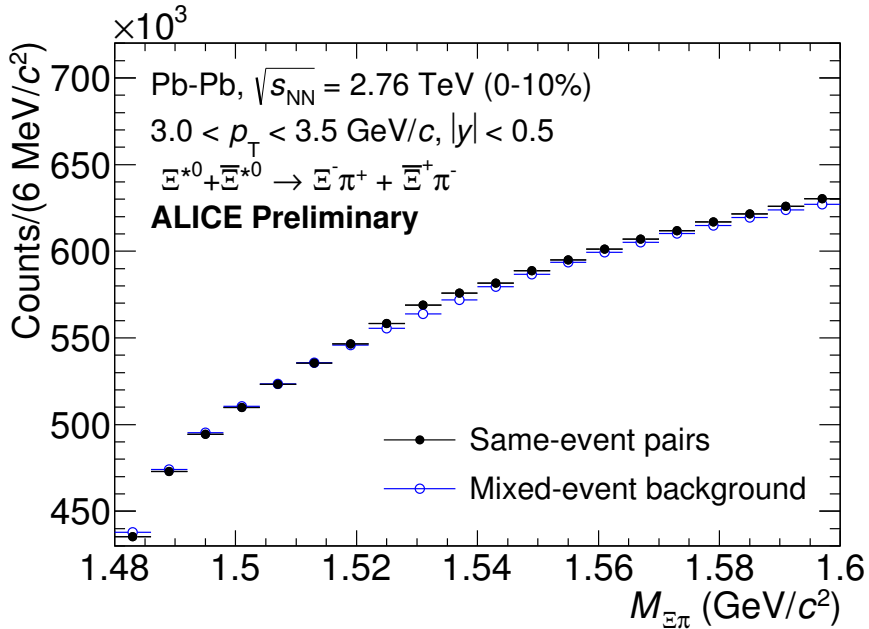


Figure 16: The $\Xi^\pm \pi^\pm$ invariant mass distribution (Same-event pairs) in $3.0 < p_T < 3.5 \text{ GeV}/c$ and for the centrality class 0-10%. The background shape, using pairs from different events (Mixed-event background), is normalised to the counts in $1.49 < M_{\Xi\pi} < 1.51 \text{ GeV}/c^2$ and $1.56 < M_{\Xi\pi} < 1.58 \text{ GeV}/c^2$.

386 the residual background and a Voigtian function (a convolution of a Breit-Wigner and a
 387 Gaussian function accounting for the detector resolution) for the signal was used. The
 388 mathematical form of fit function used in analysis is:

$$f(M_{\Xi\pi}) = \frac{Y}{2\pi} \frac{\Gamma_0}{(M_{\Xi\pi} - M_0)^2 + \frac{\Gamma_0^2}{4}} \frac{e^{-(M_{\Xi\pi} - M_0)/2\sigma^2}}{\sigma\sqrt{2\pi}} + bg(M_{\Xi\pi}) \quad (1)$$

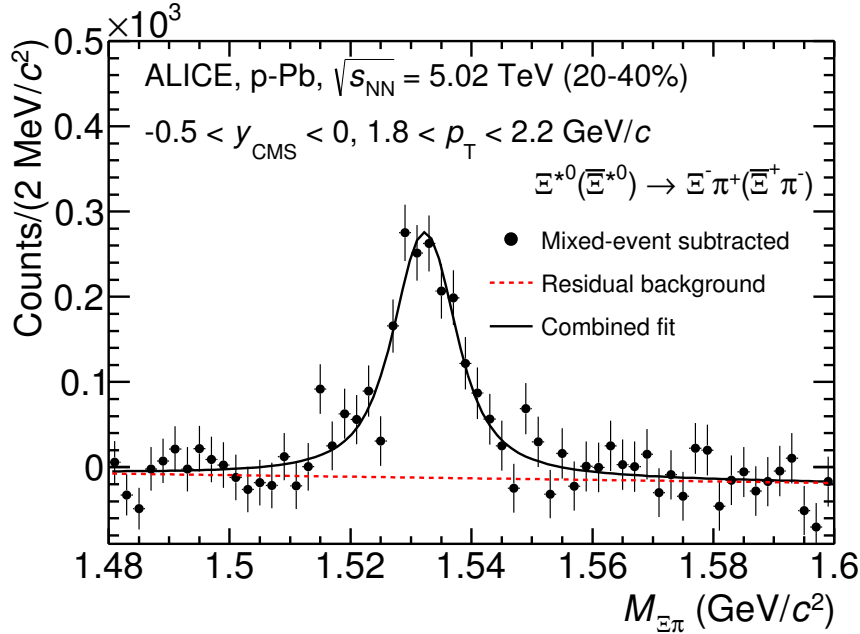


Figure 17: The invariant mass distribution after subtraction of the mixed-event background in p–Pb collisions. The solid curve represents the combined fit, while the dashed line describes the residual background.

389 The mass parameter of the Voigtian fit (M_0) is left free within the fit range ($1.48 \text{ GeV}/c^2$
 390 and $1.59 \text{ GeV}/c^2$). The overall invariant mass width of the Voigtian function is governed
 391 by 2 parameters: σ and Γ_0 . The σ describes the broadening of the peak due to finite
 392 detector resolution while Γ describes the intrinsic width of the resonance itself. The Γ_0 is
 393 fixed to the PDG value of $9.1 \text{ MeV}/c$ for the $\Xi(1530)^0$. Because of lack of statistics, the
 394 σ can be over estimated. Therefore the σ parameter is fixed to value derived from σ in
 395 MB events which has largest statistics. The σ as function of p_T distribution in MB events
 396 is shown in Figure. 19 and we also report invariant mass of $\Xi(1530)^0$ as function of p_T in
 397 Figure. 20. The $\Xi(1530)^0$ raw yields have been extracted from the fit for the 4 multiplicity

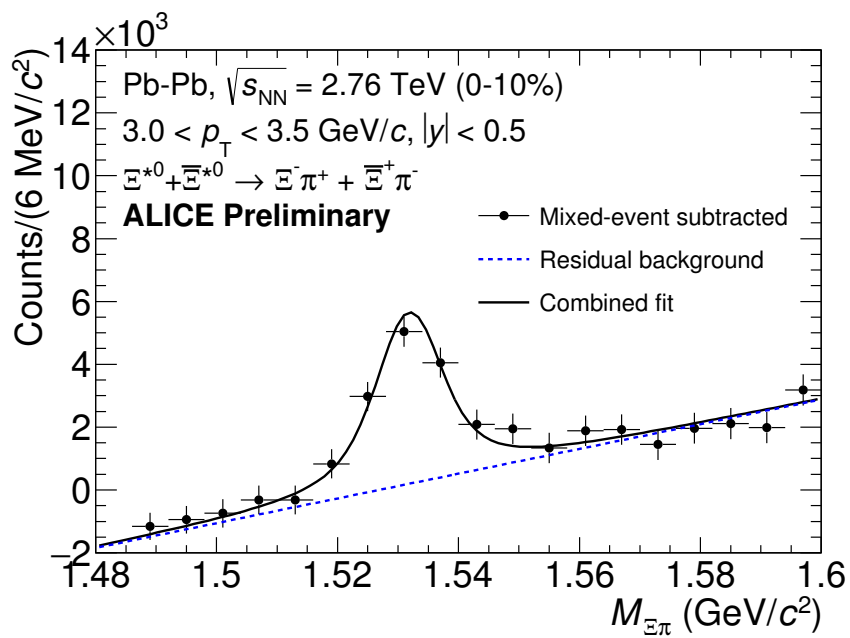


Figure 18: The invariant mass distribution after subtraction of the mixed-event background in Pb–Pb collisions. The solid curve represents the combined fit, while the dashed line describes the residual background.

³⁹⁸ bins (+1NSD events) in p–Pb and 4 centrality bins in Pb–Pb collisions and the yields as
³⁹⁹ function of p_T are shown in Figure 21.

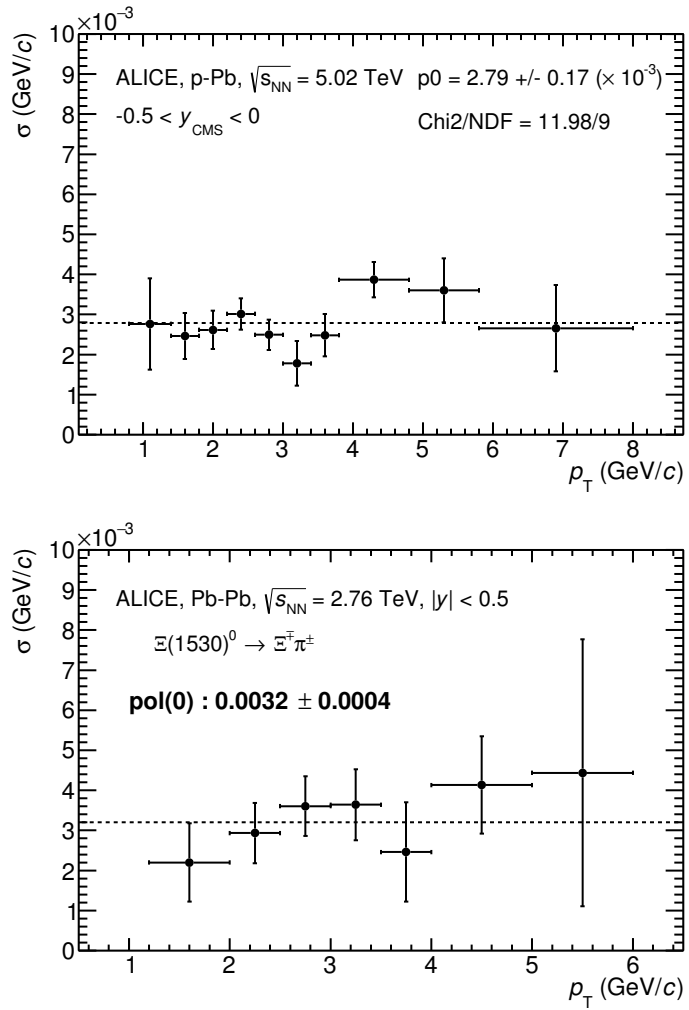


Figure 19: σ fit parameters as a function of p_T in MB in p–Pb collisions (top) and in Pb–Pb collisions (bottom).

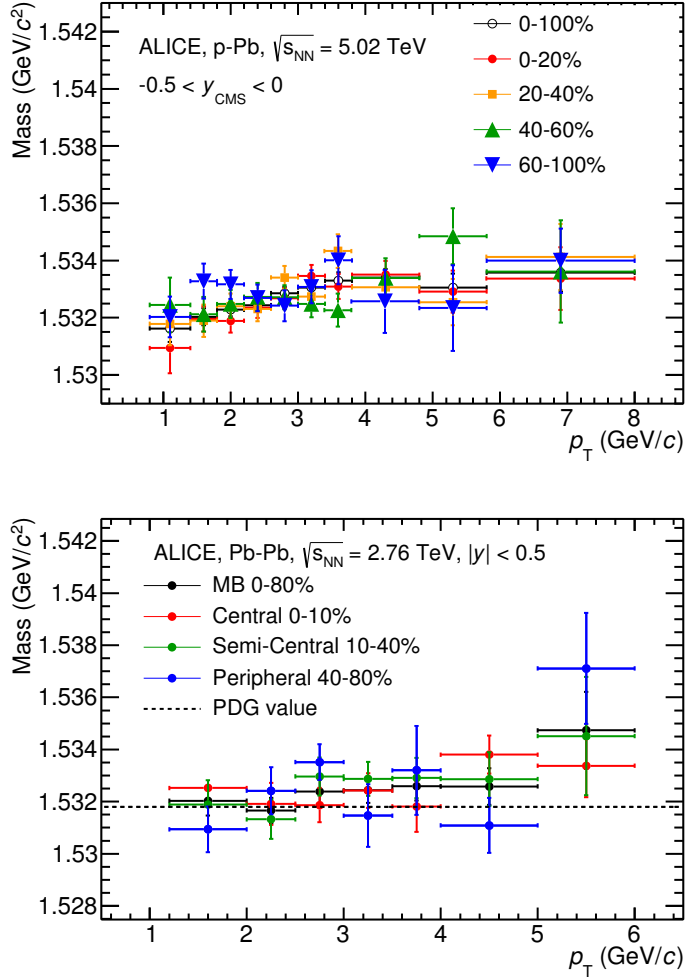


Figure 20: $\Xi(1530)^0$ -mass obtained from fit of the Voigtian peak as a function of p_T in each multiplicity classes in p-Pb collisions (top) and the different centrality classes in Pb-Pb (bottom).

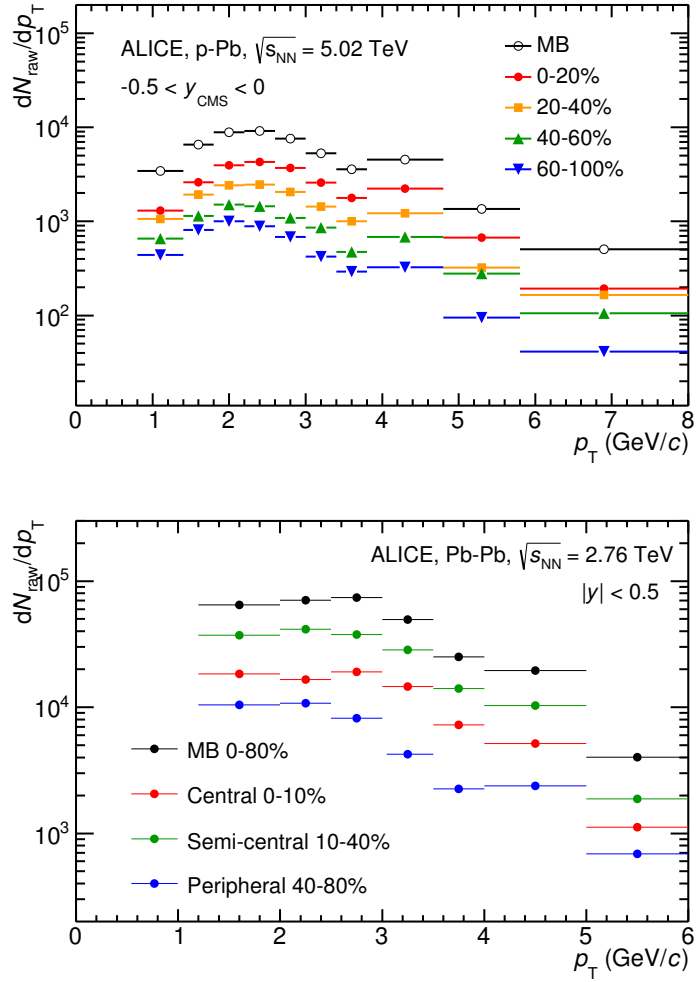


Figure 21: $\Xi(1530)^0$ -raw spectra obtained from fit of the Voigtian peak and a polynomial residual background for different multiplicities in p–Pb collisions (top) and Pb–Pb collisions (bottom). Only the statistical error is reported.

400 **5.2 Efficiency correction**

401 The raw yields were corrected for the geometrical acceptance and the reconstruction effi-
 402 ciency ($A \times \epsilon$) of the detector (Figure. 22). By using the DPMJET 3.05 event generator [17]
 403 and the GEANT 3.21 package [18], a sample of about 100 million p–Pb events was sim-
 404 ulated and reconstructed in order to compute the corrections. The distributions of $A \times \epsilon$
 405 were obtained from the ratio between the number of reconstructed Ξ^{*0} and the number of
 406 generated particle in the same p_T and rapidity interval. Since the correction factors for
 407 different multiplicity classes are in agreement with those from MB events within statistical
 408 uncertainty, the latter were used for all multiplicity classes.

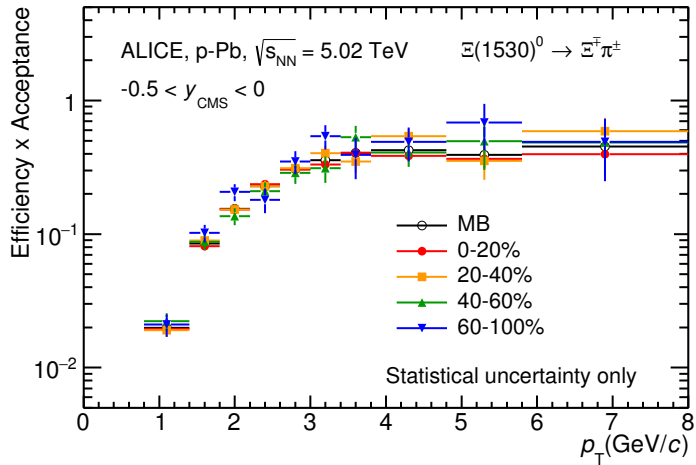


Figure 22: $\Xi(1530)^0$ -raw spectra obtained from fit of the Voigtian peak and a polynomial residual background for different multiplicities. Only the statistical error is reported.

409 Because the generated $\Xi(1530)^0$ spectra have different shapes than the measured $\Xi(1530)^0$
 410 spectra, it is necessary to weight the generated and reconstructed $\Xi(1530)^0$ spectra in these
 411 simulations. Fig. 23 shows the generated and reconstructed $\Xi(1530)^0$ spectra plotted with
 412 the (corrected) measured $\Xi(1530)^0$ spectrum for MB events and the Levy fit of that mea-
 413 sured spectrum. The generated and measured $\Xi(1530)^0$ spectra have different behaviours
 414 for the range $0.5 < p_T < 1$ GeV/ c . The generated $\Xi(1530)^0$ spectrum decreases with
 415 increasing p_T over this range, while the fit of the measured $\Xi(1530)^0$ spectrum reaches a
 416 local maximum in this range. The correction ϵ is observed to change rapidly over this
 417 p_T range. It is therefore necessary to weight the generated spectrum so that it has the
 418 shape of the measured $\Xi(1530)^0$ spectrum (and to apply corresponding weights to the re-
 419 constructed $\Xi(1530)^0$ spectrum). An iterative procedure is performed to determine the
 420 correct weighting (and therefore the correct ϵ).

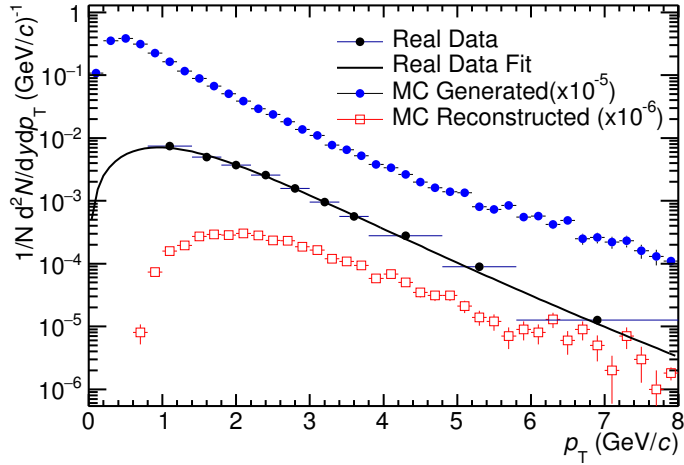


Figure 23: Real corrected $\Xi(1530)^0$ spectrum (black) for the minimum bias with Levy fit (black curve). Also shown are the unweighted generated (blue) and reconstructed (red) $\Xi(1530)^0$ spectra.

- 421 1. The unweighted ϵ is calculated.
- 422 2. This ϵ is used to correct the measured xis spectrum.
- 423 3. The corrected $\Xi(1530)^0$ spectrum is fit.
- 424 4. This fit is used to weight the simulated xis spectra. A p_T dependent weight is applied
425 to the generated xis spectrum so that it follows the fit. The same weight is applied
426 to the reconstructed xis spectrum.
- 427 5. The (weighted) ϵ is calculated.
- 428 6. Steps 2-5 are repeated (with the weighted ϵ from step 5 used as the input for step 2)
429 until the ϵ values are observed to change by $< 0.1\%$ (relative) between iterations. It
430 is observed that four iterations are sufficient for this procedure to converge.

431 Finally, the re-weighted efficiency is obtained and the distribution as function of p_T is
432 shown in Figure 24.

433 In order to obtain the correction factor dedicated in Pb-Pb collisions, MC events are
434 generated using Heavy Ion Jet Interaction Generator (HIJING). The generated events are
435 passed through a GEANT3 model of the ALICE experiment with a realistic description of
436 the detector response. Because we have observed centrality dependent efficiency, the cen-
437 trality dependent efficiencies have been applied to get corrected raw yield. The reweighting

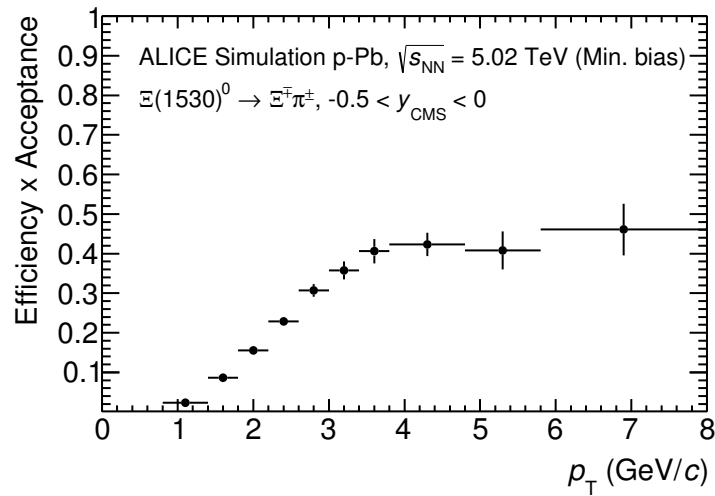


Figure 24: Efficiency as a function of p_T in minimum bias events in p–Pb collisions.

438 approach which was used to correct the efficiency in p–Pb is also applied to the efficiency
 439 obtained in Pb–Pb.

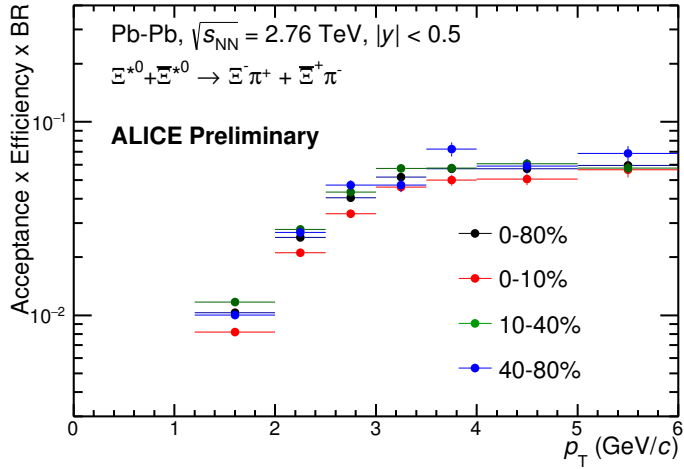


Figure 25: Efficiency as a function of p_T in different centrality classes in Pb–Pb collisions

440 5.3 Corrected p_T -spectra

441 The p_T spectrum is by the number of produced particles of a given type in the desired
 442 interval of phase-space divided by the number of inelastic collisions. The spectrum is
 443 calculated as:

$$\frac{1}{N} \times \frac{d^2N}{dydp_T} = \frac{1}{N_{E,PhysSel}} \times \frac{N_{raw}}{dp_T dy} \frac{1}{\epsilon} \frac{N_{total}^{MC}}{N_{post-PVcut}^{MC}}, \quad (2)$$

444 where N_E represent the number inelastic collisions, the $\frac{dN}{dydp_T}$ is the yield per range of
 445 rapidity y , per range in p_T . On the right hand side $N_{E,PhysSel}$ is the number of events
 446 counted by the physics selection trigger. N_{raw} is the raw extracted number of particle in the
 447 rapidity and p_T bin of width $\Delta y = 0.5$ in p–Pb ($\Delta y = 1.0$ in Pb–Pb) and Δp_T , respectively.
 448 ϵ is the reconstruction efficiency estimated from Monte Carlo simulations. $\frac{N_{total}^{MC}}{N_{post-PVcut}^{MC}}$ is the
 449 ratio of the total number of particle from MC divided by the number of particle from MC
 450 after the Primary-Vertex cut is imposed. It takes into account the fraction of particle lost
 451 after imposing the PV cut. We notice that for minimum-bias results in p–Pb, we adopted
 452 a normalisation such that to provide result from non-single diffractive(NSD) cross-section.
 453 The normalisation factor is 0.964 [2]. The obtained spectrum at MB and the spectrums
 454 from different multiplicity classes in p–Pb are shown in Figure 26 and different centrality
 455 classes in Pb–Pb are shown in Figure 27.

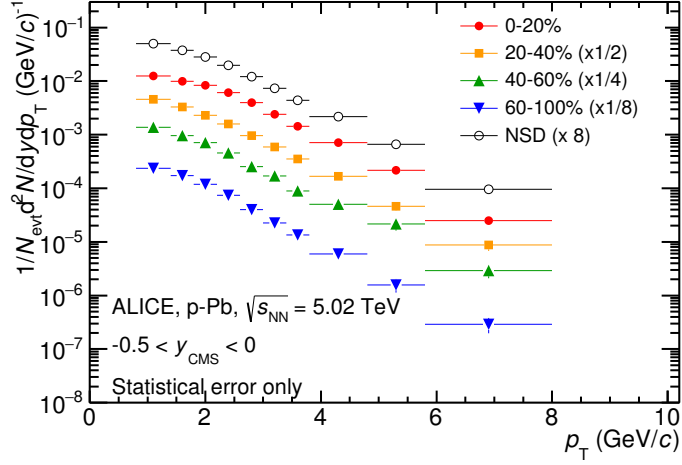


Figure 26: Corrected p_T -spectra of $\Xi(1530)^0$ in NSD and different multiplicity classes in p–Pb collisions.

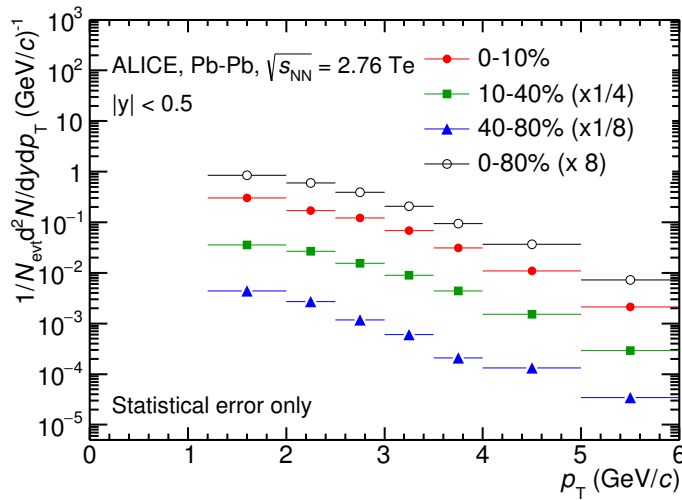


Figure 27: Corrected p_T -spectra of $\Xi(1530)^0$ in different centrality classes in Pb-Pb collisions.

456 **5.4 Systematic uncertainties**

457 The systematic uncertainties are calculated in seven principle groups. The procedure to ob-
458 tain the systematic uncertainties is performed many times by varying the possible permuta-
459 tion of the analysis parameter. The general strategy for evaluating systematic uncertainties
460 is described as following:

- 461 1. Choose one set of parameters for the analysis as default
462 2. Observe the deviation of yield when one parameter is changed
463 3. The systematic uncertainty is calculated for a given source as the RMS deviation of
464 the available sources.
465 4. The total systematic uncertainty, taking into account all the different sources, is the
466 sum in quadrature of each source.

467 To study the systematic effect we repeat the measurement by varying one parameter at
468 a time. A Barlow [19] check has been performed for each measurement to verify whether it
469 is due to a systematic effect or a statistical fluctuation. Let each measurement be indicated
470 by $(y_i \pm \sigma_i)$ and the central value (default measurement) by $(y_c \pm \sigma_c)$, one can define $\Delta\sigma_i$
471 (Eq. 3).

$$\Delta\sigma_i = \sqrt{(|\sigma_i^2 - \sigma_c^2|)} \quad (3)$$

472 Then we calculate $n_i = \Delta y_i / \Delta\sigma_i$, where $\Delta y_i = |y_c - y_i|$. If $n_i \leq 1.0$ then the effects
473 are due to the statistical fluctuation and if $n_i > 1.0$ we apply consistency check. Since
474 the alternate and default measurements are not statistically independent, an alternate
475 measurement which is statistically consistent with the default measurement should not be
476 used in calculating a systematic uncertainty. The difference between the two measurements
477 is $\Delta = y_c - y_i$. The difference in quadrature of the uncertainties is calculated by Eq. 3. It
478 could be possible to check if $\Delta < \sigma$ and exclude such cases from the systematic uncertainties.
479 However, there can be statistical fluctuations for which $\Delta > \sigma$. If the variations between the
480 default and alternate measurements are purely statistical, the distribution of Δ/σ should
481 be a Gaussian with a mean value that is consistent with zero and a deviation σ consistent
482 with unity. In this analysis, if the mean value is less than 0.1 and σ is less than 1, the
483 variation passes the consistency check.

484 Only the measurements which passed the Barlow check ($n_i > 1$) are used to determine
485 the systematic uncertainty. For measurements $N > 2$, the systematic uncertainty has been
486 determined as the RMS (eqn. 4) of the available measurements. If $N=2$, the absolute
487 difference is assigned as systematic uncertainty.

$$\delta y_{syst.} = \sqrt{\frac{1}{N} \sum_i (y_i - \bar{y})^2} \quad (4)$$

488 Here N is the total number of available measurements including y_c and \bar{y} is the average
489 of value of the measurements. The measurement did not pass Barlow check, zero systematic
490 uncertainty has been assigned to the value.

491 By suing the way as explained above, all the main contributions to the systematic un-
492 certainty of particle spectra have been studied. In particular those that comes from signal
493 extraction, topological and kinematical selection cuts, track quality selection and $n\sigma$ TPC
494 PID variation. the meaning of each source of systematic uncertainty studied is described
495 in the following:

496

497 **Signal extraction**

498 We have extracted the signal with varying the yield calculating method which contains
499 the method of signal extraction by integrating the Voigtian fit function and bin counting.
500 We also have varied the normalisation range which is related to the invariant mass region
501 where the mixed events distribution is scaled to subtract the combinatorial background
502 and different background estimator such as Like-Sign distribution and polynomial fit was
503 taken account into the systematic source of signal extraction. The systematic uncertainty
504 from signal extraction is sum in quadrature of three sources.

505

506 **Topological selection**

507 To evaluate the stability of the chosen set of values for the topological cuts, loose and tight
508 cuts have beed defined in order to vary by $\pm 10\%$ respectively. The parameters are changed
509 once at a time. Total systematic uncertainty from topological selection is calculated by
510 summation in quadrature of nine sources.

511

512 **TPC $N_{cluster}$ selection**

513 The selection performed for the daughter tracks of the cascade is that $N_{cluster}$ is larger
514 than 70 and the value has been varied to 60 and 80 in order to estimate the systematic
515 uncertainty due to this selection.

516

517 **TPC dE/dx selection**

518 In order to evaluate any potential effect due to the TPC dE/dx selection (U_{PID}), the N_σ
519 selection was varied with $N = 2.5$ and 3.5 .

520

521 **p_T shape correction**

522 As described in Section 5.2, due to the different shape of the measured and generated
523 $\Xi(1530)^0$ spectra, we have applied reweighing procedure to the generated spectra to have
524 same shape and this correction is added into contributor of systematic uncertainty as
525 p_T shape correction.

526

527 **Mass window range selection**

528 In order to select Ξ^\pm which is daughter particle of $\Xi(1530)^0$, we apply the mass window

529 ± 7 MeV/ c^2 around $\Xi(1530)^0$ mass on $\Lambda\pi$ invariant mass distribution. The boundaries
530 has been varied to ± 6 MeV/ c^2 and ± 8 MeV/ c^2 to estimate systematic uncertainty.

531

532 **Vertex range selection**

533 The distribution of vertex-z is shown in Fig.3. The cut on $|Vz|$ was varied from the nominal
534 ± 10 cm to ± 9 cm, ± 11 cm.

535

536 **Material Budget and hadronic cross section**

537 A possible source of uncertainty comes from the description of the material, active (de-
538 tecting area) or dead (structure and cable), that the particles cross during their travel in
539 the MC with respect to the real material present in the detector. Such description could
540 affect the reconstruction efficiency in different aspects (e.g. multiple scattering, energy
541 loss). The value estimated by Ξ analysis [20] has been used in this study which gives 4%
542 systematic uncertainty. In case of systematic uncertainty from hadronic cross section, we
543 have inherited the value studied in previous measurement[21] which amount is 1%.

544

545 **Tracking efficiency**

546 Systematic uncertainties from tracking efficiency from ITS + TPC combined track were
547 assigned as 3% in p–Pb and 4% in Pb–Pb collision system.[21]
548 (<https://twiki.cern.ch/twiki/bin/view/ALICE/TrackingEfficiencyCharged>)

549

550 Finally, total systematic uncertainty is sum in quadrature of sources listed above. Fig-
551 ure 28 and Figure 29 show the total systematic uncertainty in minimum bias event and
552 different multiplicity classes in p–Pb collisions, respectively. Again, Figure 30 and Figure
553 31 present the total systematic uncertainty in minimum bias event and different centrality
554 classes in Pb–Pb collisions.

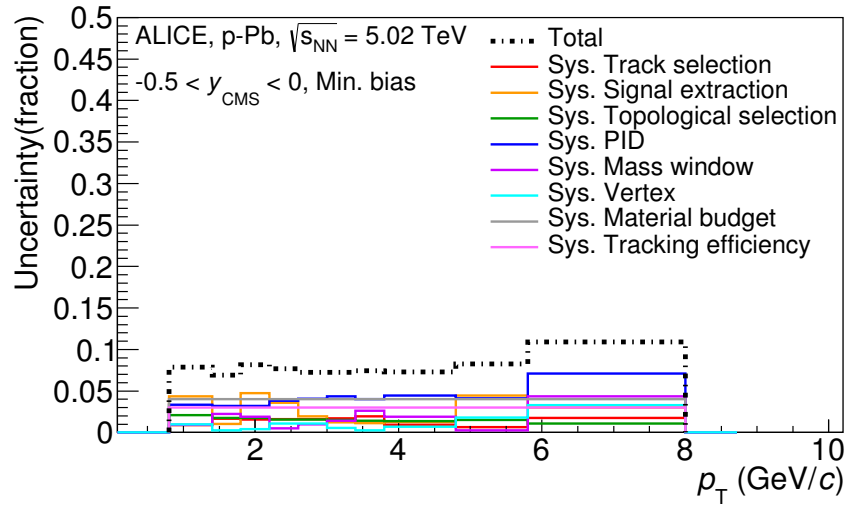


Figure 28: Summary of the contributions to the systematic uncertainty in minimum bias events in p–Pb collisions. The dashed black line is the sum in quadrature of all the contributions.

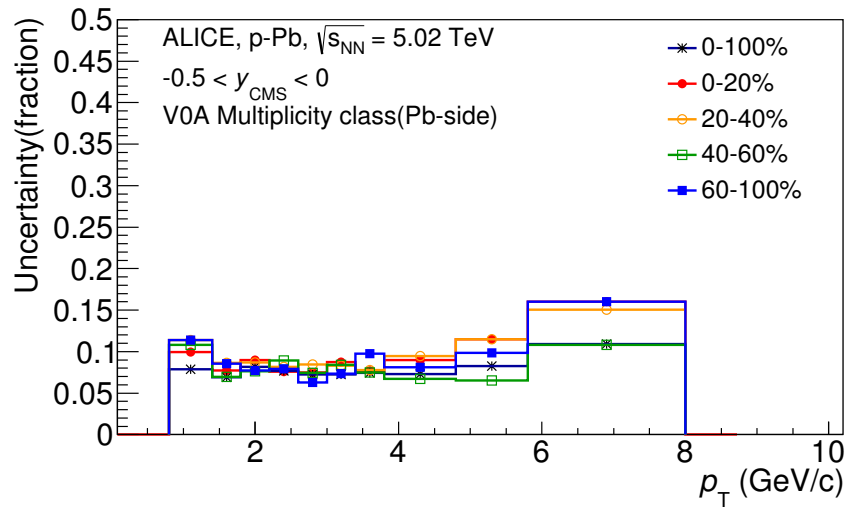


Figure 29: Systematic uncertainties for each multiplicity classes in p–Pb collisions.

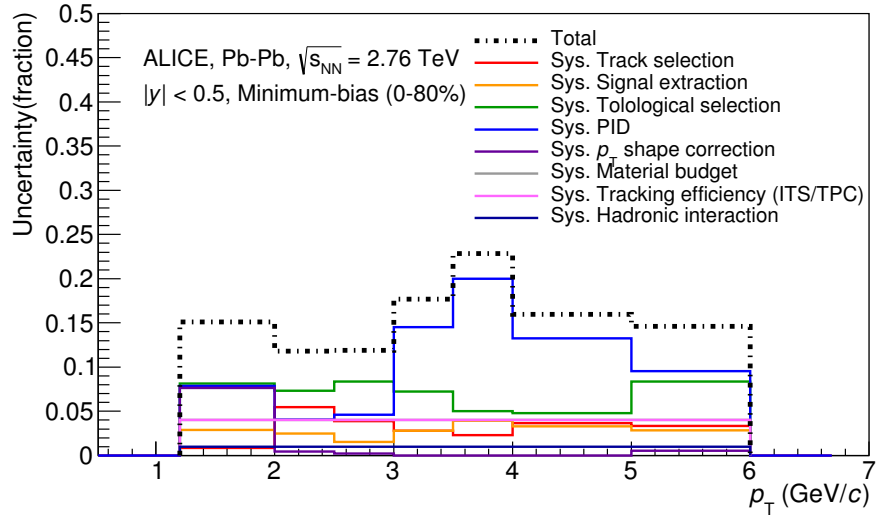


Figure 30: Summary of the contributions to the systematic uncertainty in minimum bias events in Pb–Pb collisions. The dashed black line is the sum in quadrature of all the contributions.

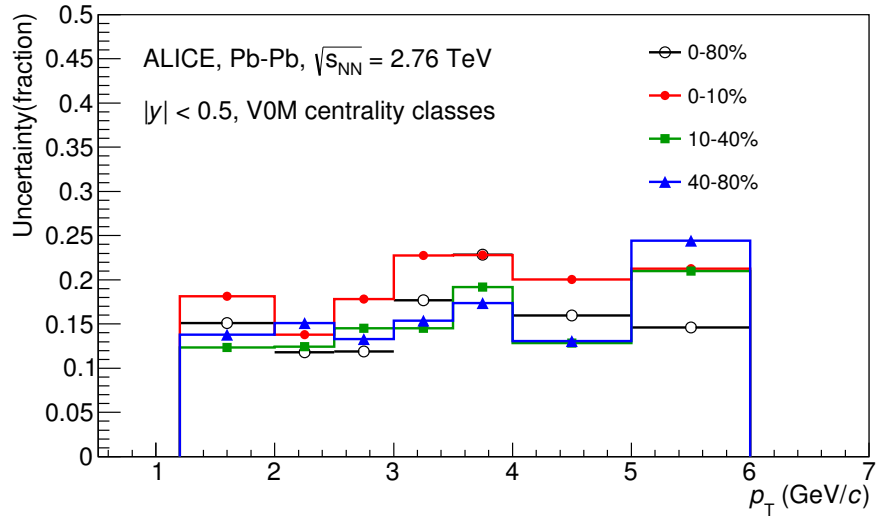


Figure 31: Systematic uncertainties for each multiplicity classes.

Source of uncertainty	$\Xi(1530)^0$ in p-Pb	$\Xi(1530)^0$ in Pb-Pb
<i>p_T-dependent</i>		
Tracking efficiency	3%	4%
Tracks selection	1-2%	1-5%
Topological selection	1-2%	5-8%
PID	3-7%	4-20%
Signal extraction	1-5%	1-4%
<i>p_T</i> shape correction	-	0-8%
Mass window (Ξ^{\pm})	4	-
Vertex selection	3%	-
<i>p_T-independent</i>		
Hadronic interaction	-	1%
Material budget	4%	4%
Branching ratio	0.3%	0.3%
Total	8-12%	9-25 %

Table 7: Summary of the systematic uncertainties on the differential yield, $d^2N/(dp_T dy)$. Minimum and maximum values in all p_T intervals and multiplicity classes in p–Pb, centrality classes in Pb–Pb are shown for each source.

555 **5.5 $\Xi(1530)^0$ transverse momentum spectra**

556 The raw yield shown in Figure 26 and 27 have been corrected for efficiency as described
 557 in section 5.2. The measured spectra for $(\Xi(1530)^0 + \bar{\Xi}(1530)^0)/2$ are reported in Figure
 558 32 for p–Pb collisions and Figure 33 for Pb–Pb collisions. The statistical and systematic
 559 uncertainties are reported respectively as the error bars and the boxes on the plot. The
 560 corrected yields for p–Pb collisions are measured with $0.8 < p_T < 8.0$ GeV/c while the
 561 yields for Pb–Pb collisions are obtained with $1.2 < p_T < 6.0$ GeV/c due to difficulty of
 562 signal extraction in low and high p_T region.

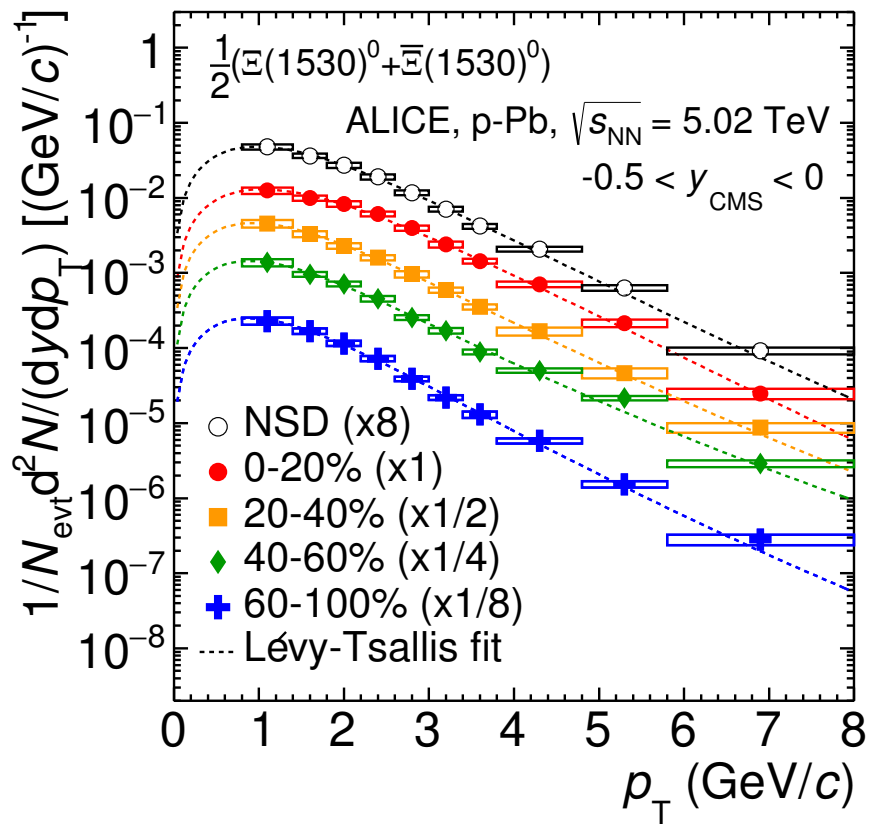


Figure 32: Corrected yields as function of p_T in NSD events and multiplicity dependent event classes in p-Pb collision system. Statistical uncertainties are presented as bar and systematical uncertainties are plotted as boxes.

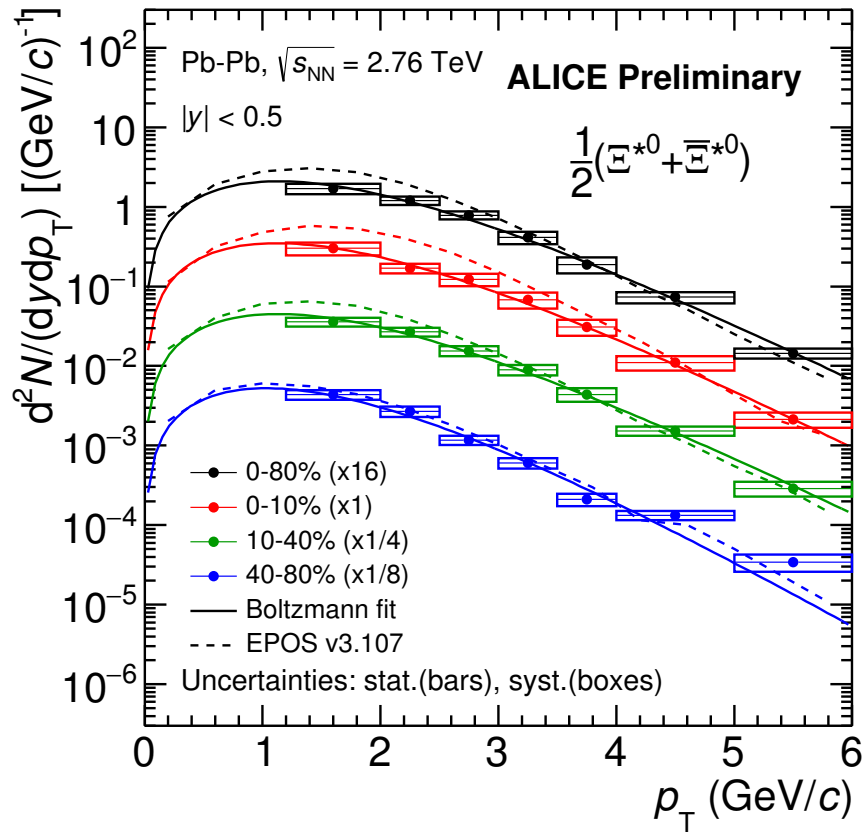


Figure 33: Corrected yields as function of p_T in different centrality classes in Pb-Pb collision system. Statistical uncertainties are presented as bar and systematical uncertainties are plotted as boxes.

563 **6 Results**

564 **6.1 Mean transverse momentum**

565 Figure 34 shows the mean transverse momentum $\langle p_T \rangle$ as a function of mean charged-
 566 particle multiplicity density $\langle dN_{\text{ch}}/d\eta_{\text{lab}} \rangle$ at midrapidity. The results for $\Xi(1530)^0$ are
 567 compared with those for other hyperons observed in p–Pb collisions at $\sqrt{s_{\text{NN}}} = 5.02$ TeV [1,
 568 3].

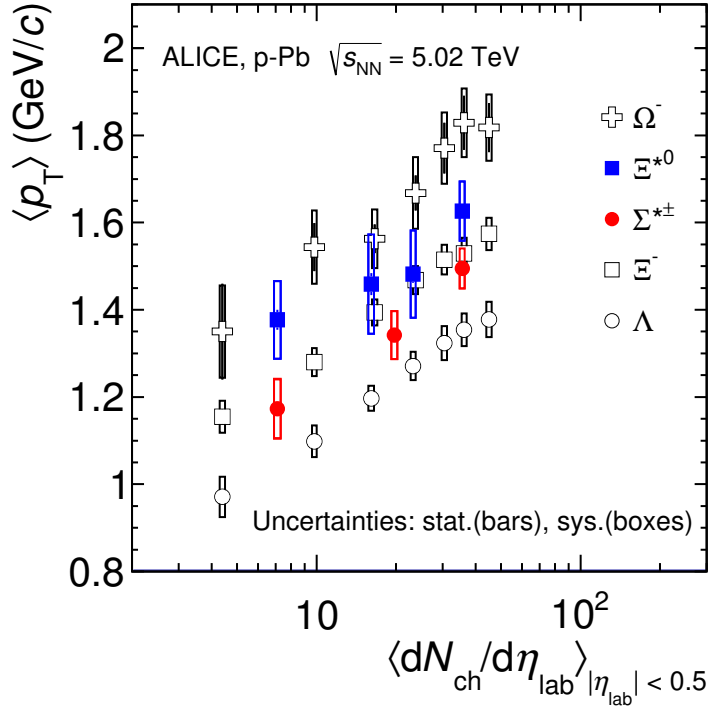


Figure 34: Mean transverse momenta $\langle p_T \rangle$ of Λ , Ξ^- , $\Sigma^{*\pm}$, Ξ^{*0} and Ω^- in p–Pb collisions at $\sqrt{s_{\text{NN}}} = 5.02$ TeV as a function of mean charged-particle multiplicity density $\langle dN_{\text{ch}}/d\eta_{\text{lab}} \rangle$, measured in the pseudorapidity range $|\eta_{\text{lab}}| < 0.5$. The results for Λ , Ξ^- and Ω^- are taken from [1, 2, 3]. Statistical and systematic uncertainties are represented as bars and boxes, respectively. The Ω^- and Ξ^- points in the 3rd and 4th lowest multiplicity bins are slightly displaced along the abscissa to avoid superposition with the $\Xi(1530)^0$ points.

569 Increasing trends from low to high multiplicities are observed for all hyperons. The
 570 mean transverse momenta increase by 20% as the mean charged-particle multiplicity in-
 571 creases from 7.1 to 35.6. This result is similar to the one obtained for the other hyperons.
 572 Furthermore, a similar increase has been observed also for K^\pm , K_S^0 , $K^*(892)^0$ and ϕ [2],

573 whereas protons are subject to a larger ($\sim 33\%$) increase in the given multiplicity range,
574 as discussed also in Ref. [1].

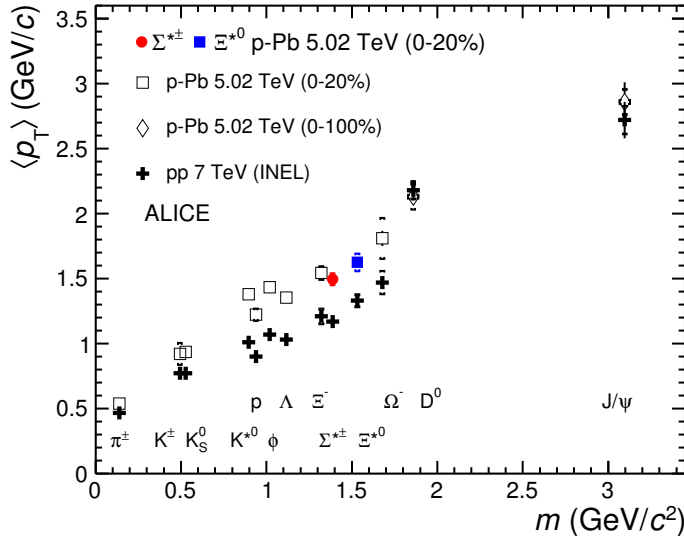


Figure 35: Mass dependence of the mean transverse momenta of identified particles for the 0 – 20% V0A multiplicity class and with $-0.5 < |y_{\text{CMS}}| < 0$ in p–Pb collisions at $\sqrt{s_{\text{NN}}} = 5.02 \text{ TeV}$ [1, 3], and in minimum-bias pp collisions at $\sqrt{s} = 7 \text{ TeV}$ [4] with $|y_{\text{CMS}}| < 0.5$. Additionally, D^0 and J/ψ results are plotted. The D^0 and J/ψ were measured in different rapidity ranges: $|y_{\text{CMS}}| < 0.5$ [5] ($|y_{\text{CMS}}| < 0.9$ [6]) for D^0 (J/ψ) in pp and $-0.96 < y_{\text{CMS}} < 0.04$ [5] ($-1.37 < y_{\text{CMS}} < 0.43$ [7]) for D^0 (J/ψ) in p–Pb. Note also that the results for D^0 and J/ψ in p–Pb collisions are for the 0-100% multiplicity class.

575 In all multiplicity classes, the $\langle p_T \rangle$ follows an approximate mass ordering: $\langle p_T \rangle_\Lambda <$
576 $\langle p_T \rangle_{\Xi^-} \simeq \langle p_T \rangle_{\Sigma^{*\pm}} < \langle p_T \rangle_{\Xi^{*0}} < \langle p_T \rangle_{\Omega^-}$. The $\langle p_T \rangle$ of $\Sigma^{*\pm}$ looks systematically lower than
577 the $\langle p_T \rangle$ of Ξ^- , despite the larger mass of $\Sigma^{*\pm}$. The uncertainties, however, are too large
578 to draw any conclusion on possible hints of violation of the mass hierarchy. This hierarchy
579 of mass-ordering, also including D^0 and J/ψ in the comparison, is displayed in Figure
580 35. Note, however, that the D^0 and J/ψ were measured in different rapidity ranges:
581 $|y_{\text{CMS}}| < 0.5$ [5] ($|y_{\text{CMS}}| < 0.9$ [6]) for D^0 (J/ψ) in pp and $-0.96 < y_{\text{CMS}} < 0.04$ [5]
582 ($-1.37 < y_{\text{CMS}} < 0.43$ [7]) for D^0 (J/ψ) in p–Pb, and the results for D^0 and J/ψ in p–Pb
583 collisions are for the 0-100% multiplicity class. This mass dependence is observed in both
584 p–Pb and pp collisions. It was observed also by the STAR collaboration [22] in MB pp,
585 MB d–Au and central Au–Au collisions.

586 Furthermore, for the light-flavour hadrons, the mean transverse momenta in p–Pb col-
587 lisions are observed to be consistently higher than those in pp collisions at 7 TeV. The

588 situation for the charm hadrons is different, where $\langle p_T \rangle$ appears compatible between both
589 colliding systems. The discrepancy is likely due to different production mechanisms for
590 heavy and light flavours and to a harder fragmentation of charm quarks. Specifically, the
591 fact that $\langle p_T \rangle$ remains similar in pp and in p–Pb is consistent with an R_{pPb} ratio com-
592 patible with unity at all p_T [5] for D^0 , and/or with the effects of shadowing in p–Pb which
593 reduces the production at low p_T and thus increasing the overall $\langle p_T \rangle$ for J/ψ [7]; the small
594 p_T hardening expected in pp when going from 5.02 to 7TeV is apparently not enough to
595 counter-balance the situation.

596 Because of small decrease of the $\langle p_T \rangle$ for proton and Λ relative to those for K^{*0} and
597 ϕ , two different trends for mesons and baryons have been suggested [23]. Even including
598 D^0 and J/ψ , as shown in Figure 35, a different trend for mesons and baryons cannot be
599 convincingly established.

600 6.2 Particle yield ratios

601 6.2.1 Comparison with other resonances

602 6.2.2 Comparison with models

603 References

- 604 [1] **ALICE** Collaboration, J. Adam *et al.*, “Multiplicity dependence of pion, kaon,
605 proton and lambda production in p–Pb collisions at $\sqrt{s_{\text{NN}}}= 5.02$ TeV,” *Phys. Lett.*
606 **B728** (2014) 25–38, [arXiv:1307.6796 \[nucl-ex\]](#).
- 607 [2] **ALICE** Collaboration, J. Adam *et al.*, “Production of $K^*(892)^0$ and $\phi(1020)$ in
608 p–Pb collisions at $\sqrt{s_{\text{NN}}}= 5.02$ TeV,” *Eur. Phys. J.* **C76** (2016) 245,
609 [arXiv:1601.7868 \[nucl-ex\]](#).
- 610 [3] **ALICE** Collaboration, J. Adam *et al.*, “Multi-strange baryon production in p–Pb
611 collisions at $\sqrt{s_{\text{NN}}}=5.02$ TeV,” *Phys. Lett.* **B758** (2016) 389–401,
612 [arXiv:1512.07227 \[nucl-ex\]](#).
- 613 [4] **ALICE** Collaboration, B. Abelev *et al.*, “Production of $\Sigma(1385)^{\pm}$ and $\Xi(1530)^0$ in
614 proton-proton collisions at $\sqrt{s}= 7$ TeV,” *Eur. Phys. J.* **C75** (2015) 1,
615 [arXiv:1406.3206 \[nucl-ex\]](#).
- 616 [5] **ALICE** Collaboration, J. Adam *et al.*, “ D -meson production in p–Pb collisions at
617 $\sqrt{s_{\text{NN}}}= 5.02$ TeV and in pp collisions at $\sqrt{s}= 7$ TeV,” *Phys. Rev. C* **94** (2016)
618 054908, [arXiv:1605.07569 \[nucl-ex\]](#).
- 619 [6] **ALICE** Collaboration, B. Abelev *et al.*, “Inclusive J/ψ production in pp collisions
620 at $\sqrt{s}= 2.76$ TeV,” *Phys. Lett.* **B718** (2012) 295–306, [arXiv:1203.3641 \[hep-ex\]](#).

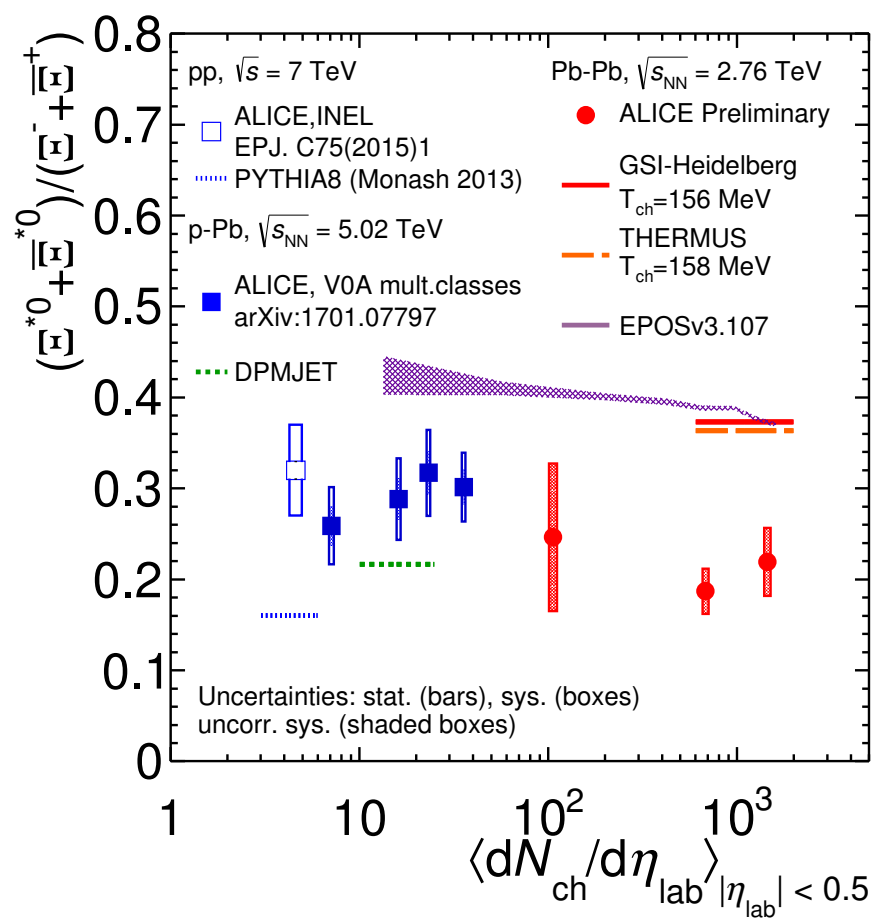


Figure 36: Integrated.

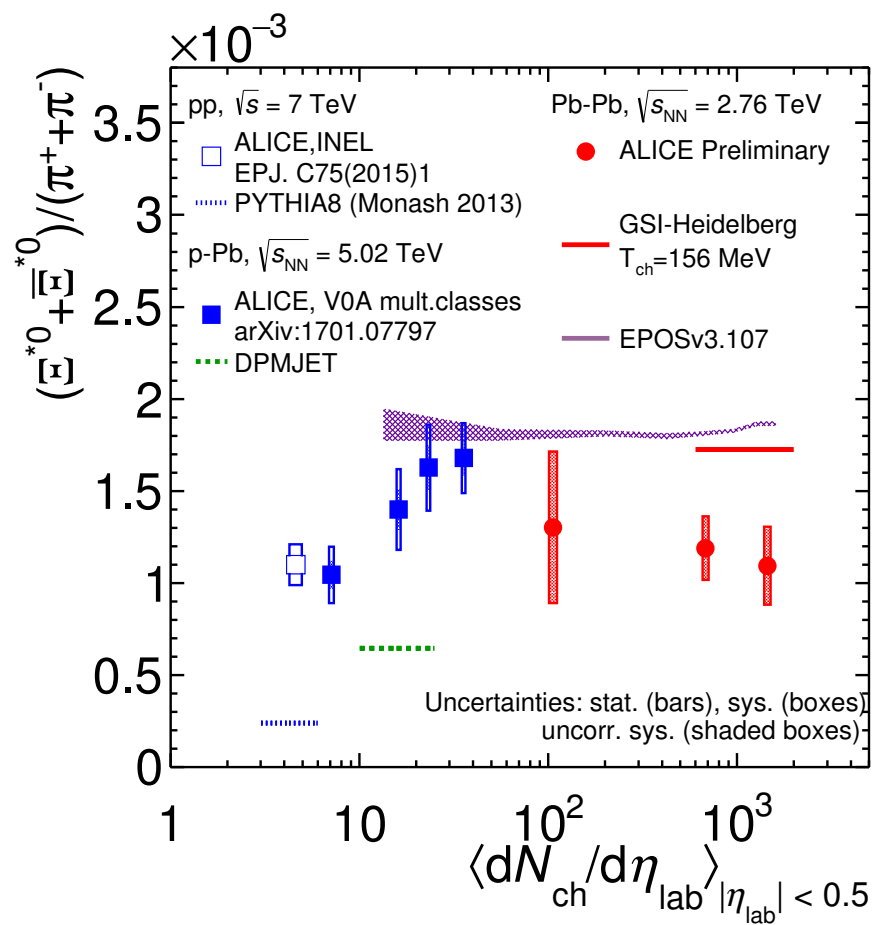


Figure 37: Integrated.

- 621 [7] **ALICE** Collaboration, J. Adam *et al.*, “Rapidity and transverse-momentum
 622 dependence of the inclusive J/ψ nuclear modification factor in p–Pb collisions at
 623 $\sqrt{s_{\text{NN}}}=5.02$ TeV,” *JHEP* **06** (2015) 55, [arXiv:1503.07179 \[nucl-ex\]](#).
- 624 [8] D. Hahn and H. Stoecker, “THE QUANTUM STATISTICAL MODEL OF
 625 FRAGMENT FORMATION: ENTROPY AND TEMPERATURE EXTRACTION
 626 IN HEAVY ION COLLISIONS,” *Nucl. Phys.* **A476** (1988) 718–772.
- 627 [9] S. Wheaton, J. Cleymans, and M. Hauer, “THERMUS: A Thermal model package
 628 for ROOT,” *Comput. Phys. Commun.* **180** (2009) 84–106, [hep-ph/0407174](#).
- 629 [10] J. Cleymans, S. Kabana, I. Kraus, H. Oeschler, K. Redlich, and N. Sharma,
 630 “Antimatter production in proton-proton and heavy-ion collisions at ultrarelativistic
 631 energies,” *Phys. Rev.* **C84** (2011) 054916, [arXiv:1105.3719 \[hep-ph\]](#).
- 632 [11] **ALICE** Collaboration, K. Aamodt *et al.*, “The ALICE experiment at the CERN
 633 LHC,” *JINST* **3** (2008) S08002.
- 634 [12] **ALICE** Collaboration, B. Abelev *et al.*, “Performance of the ALICE Experiment at
 635 the CERN LHC,” *Int. J. Mod. Phys.* **A29** (2014) 1430044, [arXiv:1402.4476](#)
 636 [nucl-ex].
- 637 [13] **ALICE** Collaboration, B. Abelev *et al.*, “Pseudorapidity Density of Charged
 638 Particles in p–Pb Collisions at $\sqrt{s_{\text{NN}}}=5.02$ TeV,” *Phys. Rev. Lett.* **110** (2013)
 639 032301, [arXiv:1210.3615 \[nucl-ex\]](#).
- 640 [14] **ALICE** Collaboration, B. Abelev *et al.*, “Centrality determination of Pb–Pb
 641 collisions at $\sqrt{s_{\text{NN}}}=2.76$ TeV with ALICE,” *Phys. Rev.* **C88** (2013) ,
 642 [arXiv:1303.0737 \[nucl-ex\]](#).
- 643 [15] **Particle Data Group** Collaboration, K. Olive *et al.*, “Review of Particle Physics,”
 644 *Chin. Phys.* **C38** (2014) 090001.
- 645 [16] **ALICE** Collaboration, K. Aamodt *et al.*, “Strange particle production in
 646 proton-proton collisions at $\sqrt{s}=0.9$ TeV with ALICE at the LHC,” *Eur. Phys. J.*
 647 **C71** (2011) 1594, [arXiv:1012.3257 \[nucl-ex\]](#).
- 648 [17] S. Roesler, R. Engel, , and J. Ranft, “The Monte Carlo Event Generator
 649 DPMJET-III, Advanced Monte Carlo for Radiation Physics, Particle Transport
 650 Simulation and Applications,” *Conference Proceedings, MC2000, Lisbon, Portugal,*
 651 *October 23-26* (2000) 1033–1038, [hep-ph/0012252](#).
- 652 [18] R. Brun, F. Carminati, and S. Giani, “GEANT detector description and simulation
 653 tool,” *CERN-W5013* (1994) .

- 654 [19] R. Barlow, “Systematic Errors: Facts and Fictions,” *Presented at Advanced*
655 *Statistical Techniques in HEP, Durham, March 2002* (2002) 333p,
656 [hep-ex/0207026v1](#).
- 657 [20] **ALICE** Collaboration, B. Abelev *et al.*, “Multi-strange baryon production at
658 mid-rapidity in Pb–Pb collisions at $\sqrt{s_{\text{NN}}}= 2.76 \text{ TeV}$,” *Phys. Lett.* **B728** (2014)
659 216–227, [arXiv:1307.5543 \[nucl-ex\]](#).
- 660 [21] **ALICE** Collaboration, B. Abelev *et al.*, “Centrality dependence of π , K and p
661 production in Pb–Pb collisions at $\sqrt{s_{\text{NN}}}= 2.76 \text{ TeV}$,” *Phys. Rev.* **C88** (2013) ,
662 [arXiv:1301.4361 \[nucl-ex\]](#).
- 663 [22] **STAR** Collaboration, B. I. Abelev *et al.*, “Hadronic resonance production in d–Au
664 collisions at $\sqrt{s_{\text{NN}}}= 200 \text{ GeV}$ measured at the BNL Relativistic Heavy-Ion Collider,”
665 *Phys. Rev.* **C78** (2008) 044906, [arXiv:0801.0450 \[nucl-ex\]](#).
- 666 [23] A. Velásquez, “Mean p_{T} scaling with m/n_q at the LHC: Absence of (hydro) flow in
667 small systems?,” *Nucl. Phys.* **A943** (2015) 9–17, [arXiv:1506.00584 \[hep-ph\]](#).

668 **Acknowledgements**